Available online at www.sciencedirect.com
ScienceDirect
Engineering Fracture Mechanics 74 (2007) 34–58
Engineering Fracture Mechanics
www.elsevier.com/locate/engfracmech

A multiscale micromechanics model for the autogenous-shrinkage deformation of early-age cement-based materials

Christian Pichler *, Roman Lackner, Herbert A. Mang

Institute for Mechanics of Materials and Structures, Vienna University of Technology, Karlsplatz 13/202, A-1040 Vienna, Austria

Available online 29 March 2006

Abstract

Autogenous shrinkage is the term for the bulk deformation of a closed, isothermal, cement-based material system not subjected to external forces [Jensen OM, Freiesleben Hansen P. Autogenous deformation and RH-change in perspective. Cement and Concrete Research 2001;31:1859–65]. It is associated with the internal volume reduction of the cement/water mixture in the course of the hydration process. The question arising from engineering practice is the magnitude of the autogenous deformations, increasing the compliance of concrete support structures and inducing tensile stresses which may lead to cracking of early-age concrete. In this paper, a multiscale model for cement-based materials focusing on the prediction of autogenous-shrinkage deformations is presented. In addition to the formulation of the underlying multiscale framework, including the identification of observation scales and the development of appropriate upscaling schemes, shrinkage experiments on cement pastes were conducted and used for the validation of the developed multiscale model. Finally, the multiscale model is used to determine the early-age elastic and shrinkage properties of shotcrete. These properties are employed in the context of hybrid analyses of shotcrete tunnel linings, providing access to the level of loading of the tunnel support structure during NATM tunneling.

Keywords: Concrete; Autogenous shrinkage; Capillary depression; Ettringite; Crystallization pressure; Multiscale modeling; Homogenization; Continuum micromechanics; Shotcrete; Hybrid analysis; Tunneling; New Austrian tunneling method (NATM)

1. Introduction

Recent advances in both experimentation and micromechanics provide the basis for the development of so-called multiscale models, incorporating finer scales of observation in the description of both biological and man-made materials. The aim of such multiscale models is to establish a relation between macroscopically

* Corresponding author.
E-mail addresses: Christian.Pichler@tuwien.ac.at (C. Pichler), Roman.Lackner@tuwien.ac.at (R. Lackner), Herbert.Mang@tuwien.ac.at (H.A. Mang).

0013-7944/$ - see front matter
doi:10.1016/j.engfracmech.2006.01.034

observable phenomena and their finer-scale origin. Once this relation is found, processes within the material can be considered at the respective observation scale and their effect on the macroscopic material performance is obtained by means of appropriate upscaling schemes. Moreover, performance-oriented optimization of the material microstructure becomes possible by modifying the material chemistry and composition.

As regards the description of the behavior of cement-based materials, the bulk of existing material models was formulated at the scale of analysis (macroscale), using macroscopic material properties (Young's modulus, compressive strength,...) as input quantities (for a review of these models, see [21,31]). As regards the description of early-age cement-based materials, macroscopic material models were developed and applied to the investigation of massive concrete components cast in place [46,14,37], and shotcrete shells obtained from spraying shotcrete onto a back-up surface [41,3,4,32]. In the mid-1990s, thermodynamics of chemically reactive porous media [44,45] was used to describe cement hydration, where the involved material properties were linked to the hydration extent by means of so-called intrinsic material functions. The mentioned hydration extent represents, in a macroscopic sense, the advance of entire set of chemical reactions taking place during cement hydration.

Recently, the description of cement hydration was reformulated by introducing four reaction extents for the four main clinker phases [7]. This refined hydration model provides access to the volume fraction of the material phases at the so-called cement-paste scale. Moreover, via upscaling in the framework of continuum micromechanics [47,48], the early-age elastic properties of cement-based materials were determined in [7].

In this paper, departing from the model proposed in [7], a multiscale material model for the prediction of macroscopic autogenous-shrinkage deformations of early-age cement-based materials is presented. In Section 2, the macroscopic observations associated with autogenous-shrinkage deformations and their finer-scale origin are described. Hereby, the loading of the microstructure, comprising the effect of capillary pressure in the liquid phase and swelling phenomena resulting from crystallization pressure, is quantified and related to the hydration extent. Upscaling of the loading situation at finer scales identified in Section 2 towards the macroscale is dealt with in Section 3. Similar to the upscaling scheme employed in [7], continuum micromechanics is applied. Experimental results obtained from uniaxial shrinkage tests of cement pastes are presented in Section 4 and the prediction capability of the developed model at the cement-paste scale is assessed. Finally, the macroscopic elastic and autogenous-shrinkage behavior, obtained from upscaling from the cement-paste scale to the macroscale (Section 3) is considered in Section 5 in the context of hybrid (macroscopic) analyses of the shotcrete lining of the Lainzer tunnel, Vienna. These analyses, performed at the structural scale, provide access to the level of loading of the tunnel lining, considering the shotcrete mixture characteristics used at the Lainzer tunnel.

2. Autogenous shrinkage—macroscopic observations and finer-scale origin

Autogenous shrinkage is associated with the internal volume reduction of the cement/water mixture caused by the hydration process. The volumetric imbalance is depicted in Fig. 1,[1] showing the phase diagram of cement paste, with f_r as the volume fraction of the different phases (adapted from [7]): the specific volume of the reaction products [calcium-silicate-hydrates (CSH), portlandite (CH), and aluminate and ferrite hydrates] is about 7% lower than the sum of the volumes of the reactants (water and cement, the latter comprising the four clinker phases C_3S, C_2S, C_3A, C_4AF and gypsum $C\overline{S}H_2$) [42], a behavior also referred to as *Le Chatelier* contraction. In Fig. 1, ξ denotes the (overall) degree of hydration, with $\xi = 1$ in case the entire amount of cement has been consumed by the hydration process [for the definition of ξ, see Appendix A (Eq. (68))]. The volumetric imbalance of 7% results in a progressive increase of the pore volume filled with the gaseous phase (see Fig. 1). On the other hand, the relative pore volume occupied by the liquid phase, i.e., the liquid saturation $f_l/(f_l + f_g)$, decreases in the course of the hydration process (see Fig. 1). The stress state in the liquid phase follows the law of surface tension: the smaller the pore size, the larger the pressure difference along the interface between the liquid and the gaseous phase. As the degree of liquid saturation

[1] Standard cement chemistry abbreviations are used throughout this paper: $C = CaO$, $S = SiO_2$, $A = Al_2O_3$, $F = Fe_2O_3$, $\overline{S} = SO_3$, $H = H_2O$.

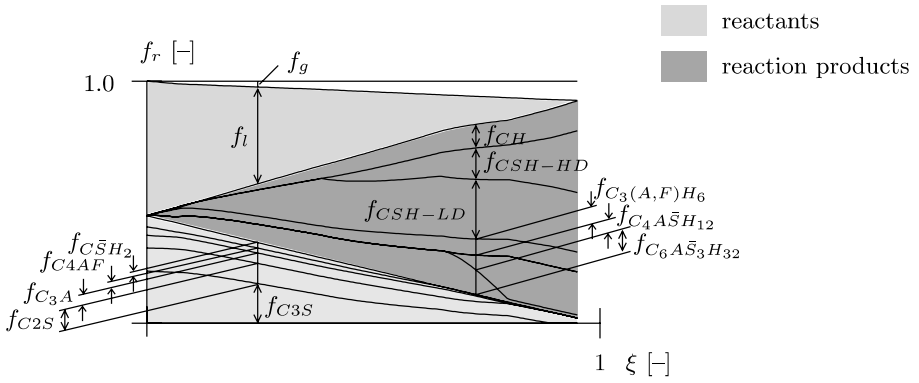

Fig. 1. Variation of volume fractions for an ordinary Portland cement (OPC) paste with $w/c = 0.4$.

decreases, the location of this interface moves into smaller pores, resulting in an increase of (capillary) depression in the liquid phase. This causes a contraction of the solid phase (unhydrated cement and reaction products), which is macroscopically observable as autogenous-shrinkage strain [2].

2.1. Capillary depression within the pore liquid

For the determination of the loading of the solid phase in consequence of capillary depression in the liquid phase, information concerning the development of the pore space in the course of hydration is required. The pore size defines the mean curvature of the liquid–gas interface $\mathbf{1}_{lg}:\mathbf{b}$ [1/m], with $\mathbf{1}_{lg}$ as the unit tensor plane to the liquid–gas interface and $\mathbf{b}$ as the tensor of curvature of the latter. Based on the *Laplace equation* [19], the capillary depression p_c, i.e., the difference between the pressure in the liquid and gaseous phase, p_l and p_g, is given by

$$-p_c = p_l - p_g = \gamma_{lg}\mathbf{1}_{lg} : \mathbf{b}, \tag{1}$$

where γ_{lg} [N/m] is the interfacial tension between the liquid and the gaseous phase. For the identification of the pore space of hardening concrete, different experimental techniques were developed:

- *Mercury intrusion porosimetry* (MIP) is characterized by the quasi-static injection of a pressurized, non-wetting fluid (mercury) into the cement paste. All evaporable pore water is removed from the pores prior to the test. MIP provides the intruded volume as a function of the applied mercury pressure. Based on the assumptions of (a) a cylindrical shape of the intruded pores and (b) a decreasing pore size with increasing distance from the outer surface of the specimen (accessibility, see case (i) in Fig. 2), the intruded pore diameter at a certain mercury pressure and, furthermore, the relative pore-size distribution can be computed

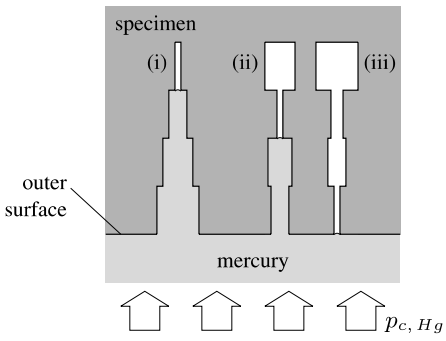

Fig. 2. Accessibility of pores by MIP.

from the intruded volume–mercury pressure relation. Unfortunately, assumption (b) cannot be confirmed by microscopic techniques [15]. A great portion of larger capillary pores is located inside the specimen and can only be reached by mercury through a chain of smaller pores of various size and shapes (see cases (ii) and (iii) in Fig. 2). Accordingly, these larger pores can only be intruded by mercury after applying a pressure which admits the intrusion of the smallest pore size encountered on that chain. The pore diameter corresponding to this pressure is referred to as "threshold" diameter. When passing the mercury pressure corresponding to the "threshold" diameter during MIP experiments, a steep increase of the intruded volume is observed. Despite the mentioned limitation of MIP, qualitative information can be extracted from experimental results, such as, e.g., the progressive refinement of the pore structure in the course of hydration [15]. Moreover, once the pressure corresponding to the "threshold" diameter is exceeded, large capillary pores inside the specimen become filled and MIP gives the correct distribution for pore sizes smaller than the "threshold" diameter. In cement pastes characterized by low water content at an advanced state of the hydration process, the liquid–gas interface is located in this pore-size range.
Specialization of Eq. (1) for a spherical-cap shaped meniscus, with

$$\mathbf{1}_{\mathrm{Hg,g}} : \mathbf{b} = \frac{1}{R_{\mathrm{Hg}}} + \frac{1}{R_{\mathrm{Hg}}} = \frac{2}{R_{\mathrm{Hg}}}, \tag{2}$$

yields an expression for the principal radius of the mercury–gas interface:

$$-p_{\mathrm{c,Hg}} = \gamma_{\mathrm{Hg,g}} \frac{2}{R_{\mathrm{Hg}}} \quad \Rightarrow \quad R_{\mathrm{Hg}} = -\frac{2\gamma_{\mathrm{Hg,g}}}{p_{\mathrm{c,Hg}}}, \tag{3}$$

with $p_{\mathrm{c,Hg}} < 0$ and $\gamma_{\mathrm{Hg,g}} = 0.474$ N/m. Accounting for the different contact angles of mercury and water with the solid phases, $\alpha_{\mathrm{Hg}} = 141°$ and $\alpha_{\mathrm{w}} \approx 0°$ (see, e.g., [22]), respectively, the principal radius of the corresponding water–gas interface can be estimated from geometric considerations as (see Fig. 3)

$$R_{\mathrm{w}} = R_{\mathrm{Hg}} \left| \frac{\cos \alpha_{\mathrm{Hg}}}{\cos \alpha_{\mathrm{w}}} \right| = -\frac{2\gamma_{\mathrm{Hg,g}}}{p_{\mathrm{c,Hg}}} \left| \frac{\cos \alpha_{\mathrm{Hg}}}{\cos \alpha_{\mathrm{w}}} \right|. \tag{4}$$

If the intruded mercury volume during MIP testing is equal to the gaseous volume of an unprepared partially saturated cement paste, the capillary pressure in this paste can be computed from Eq. (1) using R_{w} determined from Eq. (4), giving

$$p_{\mathrm{c}} = \frac{2\gamma_{\mathrm{lg}}}{R_{\mathrm{w}}}, \tag{5}$$

where $\gamma_{\mathrm{lg}} = 0.073$ N/m.

- *Nuclear magnetic resonance* (NMR) is a phenomenon observed when nuclei of certain atoms are immersed in a static magnetic field while exposing them to a second oscillating magnetic field. Under such magnetic-field conditions, some nuclei, including the protons of hydrogen in a water molecule, experience this phenomenon. One NMR measuring technique for the estimation of the pore-size distribution exploits the

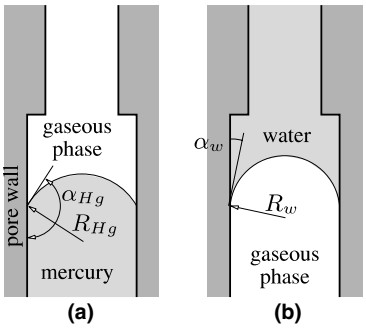

Fig. 3. Principal radii and contact angles at (a) mercury–gas and (b) water–gas interfaces.

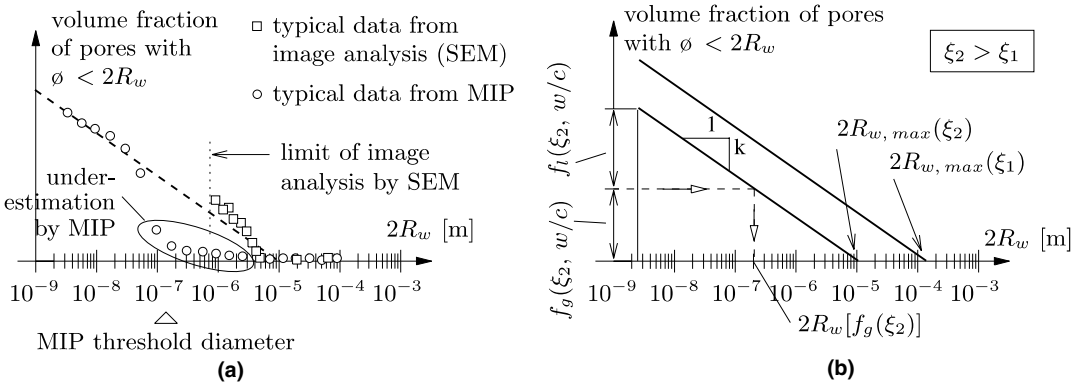

Fig. 4. Cumulative pore-size distributions obtained from MIP and image analysis: (a) typical experimental data, (b) line, fitting experimental data.

decreasing freezing temperature of water embedded in capillary pores. Hereby, the temperature of the cement specimen is continuously reduced, while the NMR signal, which is associated with the liquid part of the water, is recorded. Finally, the known relationships between the freezing-point depression and the pore size provide access to the pore-size distribution [33]. Respective pore-size distributions for a cement paste characterized by a *w*/*c*-ratio of 0.43 and a curing time of 122 days are reported in [23].

- *Image analysis* of scanning-electron-microscopy (SEM) micrographs is characterized by embedding thin slices of cement paste in low viscosity epoxy resin, polishing the surface, and detecting the epoxy filled pores in the backscatter electron images. Coverage of these pores is based on the different gray level of epoxy resin and the solid phase [16]. The lower limit of detectable pores is bound to the SEM magnification and resolution of the micrographs. In [16], pore sizes down to 8×10^{-7} m are reported. Additionally, a comparison of pore-size distributions obtained from SEM micrographs and the respective distributions from MIP measurements is given in [16]. The comparison clearly shows the aforementioned underestimation of the portion of larger pore sizes, with diameters above the "threshold" diameter, when employing MIP [see Fig. 4(a)].
- Pore-size distributions can also be obtained by the analysis of *water vapor adsorption isotherms*. In this experiment, the specimen is placed into a sealed cell, where the relative humidity is controlled and increased in a step-wise manner [5]. Combining the *Kelvin equation*[2] and Eq. (5), the radius of the liquid–gas interface becomes a function of the relative humidity. Considering the change of the specimen weight during adsorption experiments, the radius can be related to the volume fraction of the water.

Fig. 4(a) shows typical data obtained from MIP and image analysis of vacuum mixed cement pastes, characterized by no initial porosity, i.e., $f_g(\xi = 0) = 0$. Taking into account that MIP measurements provide reliable results for small pore sizes and image analysis is limited to greater pore-size ranges, a line approximating the respective ranges of the pore size is introduced [see Fig. 4(b)]. Based on experimental data of cement pastes characterized by various values of the *w*/*c*-ratio and ξ [13,16], the slope of the line was identified as $k = 0.2/\log_{10}(3 \times 10^{-7}/1 \times 10^{-8}) = 0.135$, starting from a pore diameter of 2.5×10^{-9} m. According to [9], the latter corresponds to the smallest pore size, at which menisci can form. The linear approximation of the cumulative pore-size distribution allows determination of the pore radius at the liquid–gas interface for a given volume fraction of the gaseous phase $f_g(\xi, w/c)$ [see Fig. 4(b)]. For the so-obtained value of $2R_w(f_g)$, the capillary

[2] The *Kelvin equation* expresses the liquid–vapor equilibrium under atmospheric conditions:

$$p_c = -\frac{\rho_H \mathscr{R} T}{\mathscr{M}_H} \ln h, \tag{6}$$

where ρ_H is the liquid density, $\mathscr{R}$ is the universal gas constant, T is the absolute temperature, $\mathscr{M}_H$ is the molar mass of water, and h is the relative humidity.

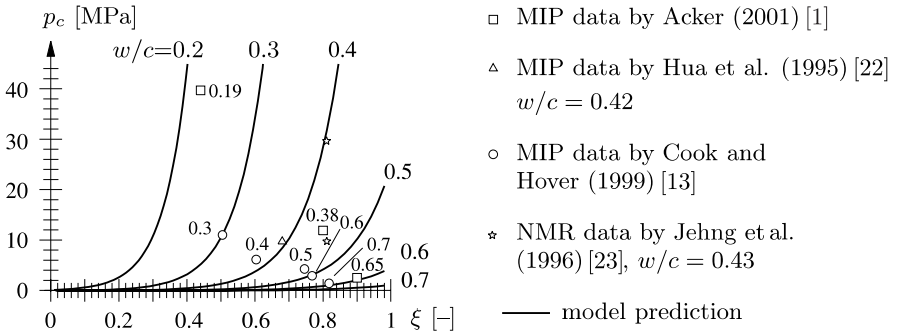

Fig. 5. Capillary pressure as a function of the w/c-ratio and ξ.

Table 1
Determination of p_c for specific values of the w/c-ratio and ξ

1. Determination of f_l and f_g from the given values for the w/c-ratio and ξ on the basis of the relations given in Fig. 1 (see also Appendix A)
2. Use of the linear relationship in Fig. 4(b) for determination of $R_{w,max}$ and, subsequently of $R_w(f_g)$ from the relations (i) $k = (f_g + f_l)/[\log_{10}(2R_{w,max}) - \log_{10}(2.5 \times 10^{-9})]$ giving $-R_{w,max}(f_g + f_l)$, and (ii) $k = f_g/[\log_{10}(2R_{w,max}) - \log_{10}(2R_w(f_g))]$ giving $R_w(f_g)$, where $k = 0.135 = \text{const.}$ and f_l and f_g are obtained from Step 1
3. Determination of p_c from $R_w(f_g)$ using Eq. (5)

pressure of the pore liquid can be computed from Eq. (5). This approach for determining the capillary depression was assessed by four different data sets reported in the open literature [1,22,13,23]. Fig. 5 shows the comparison of these test data and the model prediction based on $k = 0.135$ and Eq. (5). The model result for p_c as a function of the w/c-ratio and ξ were obtained from the calculation scheme outlined in Table 1.

2.2. Crystallization pressure due to ettringite formation

A counteracting, i.e., expansive behavior frequently observed in autogenous-shrinkage measurement right after setting is explained by the formation pressure of crystalline ettringite $C_6A\overline{S}_3H_{32}$, resulting from tricalcium aluminate C_3A hydration in the presence of gypsum (see Appendix A). Whereas hydration of tricalcium silicate C_3S and dicalcium silicate C_2S is a through solution reaction – the clinker phases dissolve in the pore solution and the hydration products (CSH) precipitate from the solution and attach to the existing load-bearing solid framework of the material in a state free of stress [6], ettringite formation is a solid–liquid or topochemical reaction. The space locally available at the C_3A surface is not big enough to accommodate the newly formed ettringite crystal.[3] According to [39], the crystallization pressure of ettringite resulting from this spatial constraints is given by

$$p_{C_6A\overline{S}_3H_{32}} = \frac{\mathscr{R}T}{\mathscr{M}_{C_6A\overline{S}_3H_{32}}/\rho_{C_6A\overline{S}_3H_{32}}} \ln \Omega, \tag{7}$$

where $\mathscr{R} = 8.3144\ \text{N m/(mol K)}$ is the universal gas constant, T [K] is the absolute temperature, $\mathscr{M}_{C_6A\overline{S}_3H_{32}}/\rho_{C_6A\overline{S}_3H_{32}} = 71.7 \times 10^{-5}\ \text{m}^3/\text{mol}$ is the molar volume of the solid product, i.e., ettringite, and Ω is the solubility product ratio. The latter is given by $\Omega = K/K_0$, where K_0 and K are the solubility products under atmospheric pressure p_0 and solid phase pressure $p_0 + p_{C_6A\overline{S}_3H_{32}}$, respectively. According to [39],

[3] As reviewed in [12], two explanations for the expansion in the course of ettringite formation exist: (1) expansion is caused by the growth of ettringite crystals which form on the surfaces of C_3A particles or in the solution. Crystal growth is responsible for the crystallization pressure and, hence, for the expansive forces. (2) Expansion is due to swelling of the ettringite particles, which are of colloidal size and characterized by a large specific surface area. The formation of this gel occurs as a through solution reaction. Considering the experimental setup employed in this paper (see Section 4), characterized by cement-paste specimens under sealed conditions (no external water supply), the first explanation seems favorable.

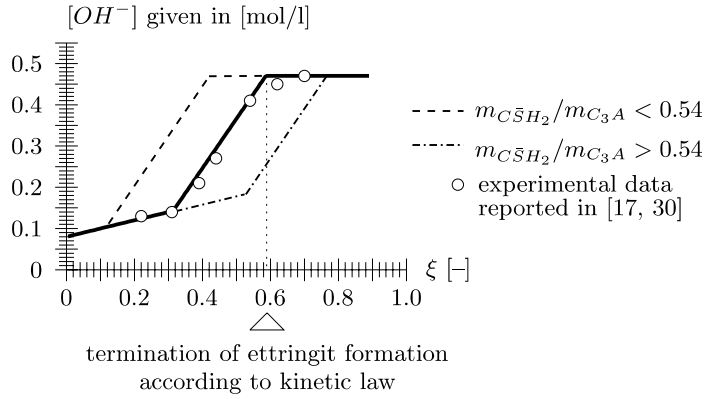

Fig. 6. OH^- concentration as a function of ξ.

$$\frac{\mathrm{d}\ln\Omega}{\mathrm{d}\ln\{[\mathrm{OH}^-]/(\mathrm{mol/l})\}} = -8, \tag{8}$$

where $[OH^-]/(mol/l)$ is the so-called activity with $[OH^-]$ given in [mol/1] as the concentration of OH^- in the pore solution. According to Eq. (8), an increase of $[OH^-]$, reflecting a decrease of sulfate concentration, $[SO_4^{2-}]$, results in a decrease of the solubility product ratio Ω and, thus, in a decrease of the crystallization pressure [see Eq. (7)]. Inserting the integrated form of Eq. (8) into Eq. (7), one gets the ettringite crystallization pressure as a function of $[OH^-]$, reading

$$p_{\mathrm{C_6A\bar{S}_3H_{32}}} = -\frac{\mathscr{R}T}{\mathscr{M}_{\mathrm{C_6A\bar{S}_3H_{32}}}/\rho_{\mathrm{C_6A\bar{S}_3H_{32}}}} 8\ln\{[\mathrm{OH}^-]/(\mathrm{mol/l})\}. \tag{9}$$

Studies on the evolution of $[OH^-]$ in OPC paste show a steep increase to approximately 0.080 mol/l within the first hour of hydration [42]. Fig. 6 contains the evolution of $[OH^-]$ for OPC characterized by $w/c = 0.45$ and a ratio of mass fraction of gypsum to tricalcium aluminate of $m_{\mathrm{C\bar{S}H_2}}/m_{\mathrm{C_3A}} = 5.3/9.8 = 0.54$ [17,30]. The more solid gypsum is present in the system and, thus, the higher the sulfate concentration, $[SO_4^{2-}]$, the longer the increase of $[OH^-]$ is retarded [17]. Fig. 6 shows the evolution of $[OH^-]$ as a function of the overall degree of hydration ξ [for the definition of ξ, see Appendix A (Eq. (68))]. The upper corner of the curves depicted in Fig. 6 corresponds to the termination of ettringite formation and, hence, to the consumption of gypsum (i.e., the end of the first stage of C_3A hydration, see Appendix A).

3. Multiscale material model for autogenous shrinkage

3.1. Observation scales and modeling of microstructure

The employed multiscale model for upscaling of elastic and autogenous-shrinkage properties of cement-based materials comprises four length scales, which are identified as (see Fig. 7):

- Scale I comprises the four clinker phases, high-density CSH (CSH-HD) and low-density CSH (CSH-LD), and the water and air phase. The four clinker phases, which do not exhibit time-dependent behavior, are condensed into one material phase (Scale Ia). The constituents showing time-dependent behavior, on the other hand, are combined at Scale Ib.1, where CSH-HD is located in the space confined by the previously formed CSH-LD. At the porous CSH scale (Scale Ib.2), water and air are considered as inclusions in a matrix constituted by the homogenized material of Scale Ib.1.
- At Scale II (*cement-paste scale*), anhydrous cement (homogenized material of Scale Ia), gypsum $C\bar{S}H_2$, portlandite CH, and reaction products from C_3A and C_4AF hydration [see right-hand side of Eqs. (54)–(57) in Appendix A] form inclusions in a matrix constituted by the homogenized material of Scale Ib.2.

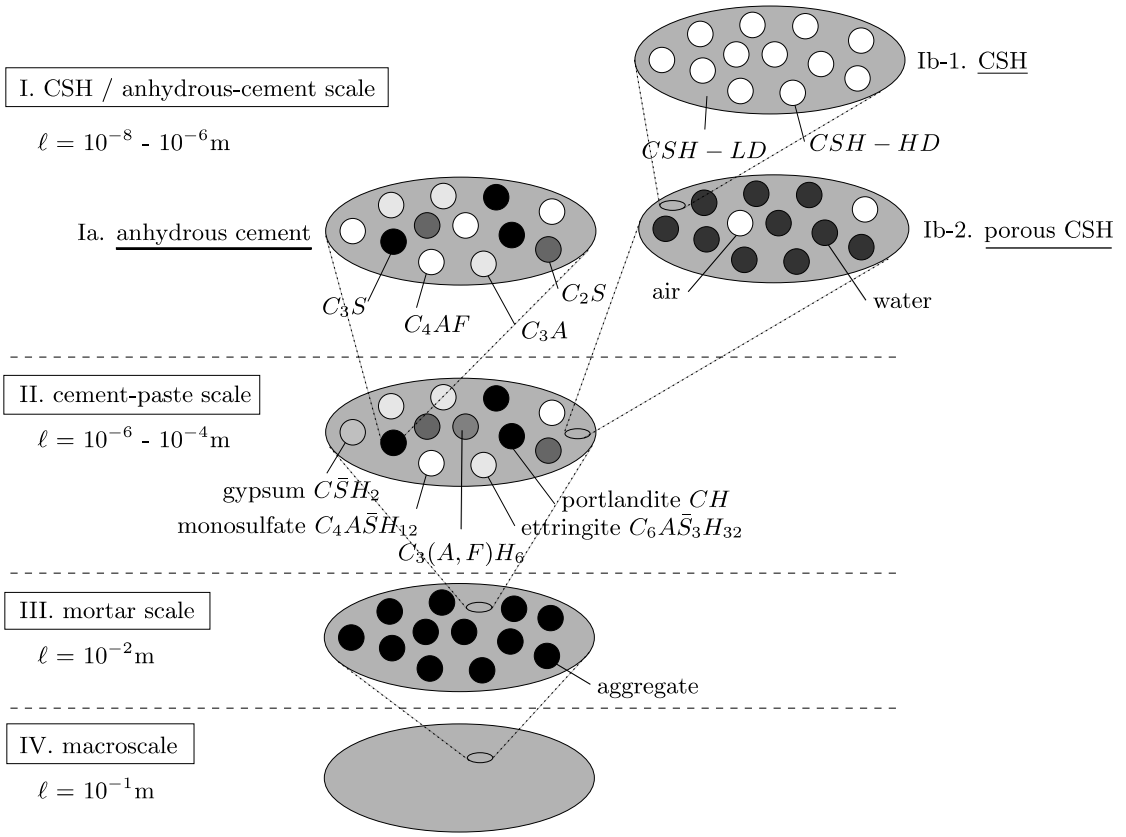

Fig. 7. Scales of observation for upscaling of properties of cement-based materials [ℓ = size of representative volume element (RVE)].

- At Scale III (*mortar or concrete scale*), aggregates are represented as inclusions in the cement paste (homogenized material of Scale II).
- Finally, at Scale IV (*macroscale*), concrete is treated as a continuum.

The four length scales obey the separability of scale condition, i.e., they are separated one from each other by at least one order of magnitude. For upscaling of information from the finer scales towards the macroscale, continuum micromechanis is employed. Hereby, the self-consistent scheme [26,20] is used for homogenization at Scale Ia. For homogenization at Scales Ib to III, on the other hand, the matrix-inclusion type morphology is taken into account by using the Mori–Tanaka homogenization scheme [34]. The volume fractions at the different length scales entering the homogenization schemes are obtained from the kinetic models outlined in Appendix A.

3.2. Consideration of capillary depression at Scale Ib.2 (porous CSH scale) according to [11]

The effect of prestress in the liquid and gaseous phase is considered during homogenization at Scale Ib.2. Hereby, the prestress field $\boldsymbol{\sigma}_p$ is given as

$$\boldsymbol{\sigma}_p(\mathbf{x}) = \begin{cases} -\mathbf{1}p_l & \text{for } \mathbf{x} \in V_l, \\ -\mathbf{1}p_g & \text{for } \mathbf{x} \in V_g, \\ \mathbf{0} & \text{for } \mathbf{x} \in V_s, \end{cases} \tag{10}$$

where p_l and p_g are the liquid and gaseous pressure, respectively. In addition to the prestress field in the liquid and gaseous phase given in Eq. (10), the membrane forces at the different interfaces between phases are taken

into account. By relating the stress tensor to the curvature of the interface, these membrane forces are represented by

$$\begin{aligned}&\text{solid–liquid interface:}\quad \boldsymbol{\sigma}_s\cdot\mathbf{n}=-p_l\mathbf{n},\\ &\text{solid–gas interface:}\quad \boldsymbol{\sigma}_s\cdot\mathbf{n}=-p_g\mathbf{n}-\gamma_{sg}(\mathbf{1}_{sg}:\mathbf{b})\mathbf{n},\\ &\text{liquid–gas interface:}\quad \gamma_{lg}\mathbf{1}_{lg}:\mathbf{b}=p_l-p_g=-p_c\quad[\text{see also Eq. (5)}],\end{aligned}\tag{11}$$

where $\mathbf{n}$ is the unit-normal vector, $\mathbf{1}_{sg}$ and $\mathbf{1}_{lg}$ represent the unit tensor plane to the solid–gas and liquid–gas interface, respectively, $\mathbf{b}$ is the tensor of curvature of the respective interface. Assuming that the liquid perfectly wets the solid (implying a contact angle of $\alpha_l=0$), the surface tension at the solid–gas interface, γ_{sg}, is set equal to the surface tension of the liquid–gas interface, with $\gamma_{sg}=\gamma_{lg}=0.073$ N/m. Based on *Hill's* lemma[4] [10], the macroscopic prestress tensors related to the prestress field and interface-stress tensor, $\boldsymbol{\Sigma}_p$ and $\boldsymbol{\Sigma}_{int}$, respectively, take the form

$$\boldsymbol{\Sigma}_p=-f_l p_l\mathbf{1}:\langle\mathbb{A}\rangle_l-f_g p_g\mathbf{1}:\langle\mathbb{A}\rangle_g,\tag{13}$$

$$\boldsymbol{\Sigma}_{int}=-\int_{\partial V_{sg}}\gamma_{sg}(\mathbf{x})\mathbf{1}_{sg}:\mathbb{A}\,\mathrm{d}(\partial V),\tag{14}$$

where $\mathbb{A}$ is the fourth-order strain-localization tensor.

Accounting for isomorphology of the liquid and gaseous phase, i.e., $\langle\mathbb{A}\rangle_l=\langle\mathbb{A}\rangle_g=\langle\mathbb{A}\rangle_p$, and employing virtual work relations, the membrane force γ_{sg} in Eq. (14) is transferred into a work-equivalent pressure $p_{\partial V}$ within the gaseous phase. The virtual work corresponding to the surface tension γ_{sg} is given by

$$\widetilde{W}=\int_{\partial V_{sg}}\gamma_{sg}\mathbf{1}_{sg}:\tilde{\mathbf{e}}\,\mathrm{d}(\partial V)=\int_{\partial V_{sg}}\gamma_{sg}\mathbf{1}_{sg}:\tilde{\boldsymbol{\varepsilon}}\,\mathrm{d}(\partial V),\tag{15}$$

where the virtual strain field $\tilde{\mathbf{e}}$, which is related to the virtual displacement field, $\tilde{\mathbf{u}}$, is replaced by the virtual membrane strain $\tilde{\boldsymbol{\varepsilon}}$. Expressing $\tilde{\boldsymbol{\varepsilon}}$ by the virtual displacement field, $\tilde{\mathbf{u}}$, one gets

$$\widetilde{W}=\int_{\partial V_{sg}}\gamma_{sg}(\mathbf{1}_{sg}:\mathbf{b})\mathbf{n}\cdot\tilde{\mathbf{u}}\,\mathrm{d}(\partial V).\tag{16}$$

Replacing the mean curvature $\mathbf{1}_{sg}:\mathbf{b}$ in Eq. (16) by $-2/R_w(f_g^{II})$, where R_w is given by the volume fraction of the gaseous phase at Scale II [see Fig. 4(b)], and introducing the pressure acting at the solid–gas interface as $p_{\partial V}=2\gamma_{sg}/R_w(f_g^{II})$ [see Eq. (5)], the virtual work $\widetilde{W}$ becomes a function of $p_{\partial V}$, reading

$$\widetilde{W}=-\int_{\partial V_{sg}}p_{\partial V}\mathbf{n}\cdot\tilde{\mathbf{u}}\,\mathrm{d}(\partial V).\tag{17}$$

Assuming spherical inclusions, the virtual work of a pressure acting on ∂V_{sg} resulting from a virtual radial displacement $\mathbf{n}\cdot\tilde{\mathbf{u}}$ is equal to the the virtual work resulting from this pressure in consequence of a virtual volumetric strain $\mathbf{1}:\tilde{\mathbf{e}}$, giving

$$\widetilde{W}=-\int_0^{f_g}p_{\partial V}\mathbf{1}:\tilde{\mathbf{e}}\,\mathrm{d}f.\tag{18}$$

Finally, comparing Eqs. (18) and (15), the surface integral in Eq. (14) can be replaced by $-\int_0^{f_g}p_{\partial V}\mathbf{1}:\langle\mathbb{A}\rangle_p\,\mathrm{d}f$, yielding

$$\boldsymbol{\Sigma}_{int}=\int_0^{f_g}p_{\partial V}\mathbf{1}:\langle\mathbb{A}\rangle_p\,\mathrm{d}f.\tag{19}$$

[4] According to *Hill's* lemma,

$$\boldsymbol{\Sigma}:\mathbf{E}=\langle\boldsymbol{\sigma}\rangle_V:\langle\boldsymbol{\varepsilon}\rangle_V=\langle\boldsymbol{\sigma}:\boldsymbol{\varepsilon}\rangle_V,\tag{12}$$

where $\boldsymbol{\sigma}(\mathbf{x})$ is equilibrated and $\boldsymbol{\varepsilon}(\mathbf{x})$ is compatible, i.e., derived from a displacement field, and either the former or the latter obeys homogeneous boundary condition [48]. In Eq. (12), $\langle\bullet\rangle_V=1/V\int_V\bullet\,\mathrm{d}V$.

Rewriting the obtained result for the homogenized prestress tensor $\mathbf{\Sigma}_{\mathrm{p}}$ and the homogenized interface-stress tensor $\mathbf{\Sigma}_{\mathrm{int}}$ in volumetric form, one gets

$$\operatorname{tr}\mathbf{\Sigma}_{\mathrm{p}} + \operatorname{tr}\mathbf{\Sigma}_{\mathrm{int}} = -f_{\mathrm{l}}p_{\mathrm{l}}\langle A\rangle_{\mathrm{p}} - f_{\mathrm{g}}p_{\mathrm{g}}\langle A\rangle_{\mathrm{p}} + \langle A\rangle_{\mathrm{p}}\int_0^{f_{\mathrm{g}}} p_{\partial V}\,\mathrm{d}f. \tag{20}$$

In Eq. (20), $\langle A\rangle_{\mathrm{p}}$ denotes the volumetric average of the strain localization tensor in the liquid and gaseous phase (embedded in the solid matrix s):

$$\langle A\rangle_{\mathrm{p}} = \left[(1-S)\sum_r \frac{f_r}{1+S\frac{k_r-k_{\mathrm{s}}}{k_{\mathrm{s}}}}\right]^{-1}, \tag{21}$$

with $r \in \{l,g,s\}$. In Eq. (21), S represents the Eshelby tensor $\mathbb{S}$ specialized for spherical inclusions embedded in the solid matrix (see, e.g., [36])

$$S_{ijkl} = \frac{5\nu_{\mathrm{s}}-1}{15(1-\nu_{\mathrm{s}})}\delta_{ij}\delta_{kl} + \frac{4-5\nu_{\mathrm{s}}}{15(1-\nu_{\mathrm{s}})}(\delta_{ik}\delta_{jl}+\delta_{il}\delta_{jk}), \tag{22}$$

giving $S = S_{iiii} + 2S_{iijj} = 1/3(1+\nu_{\mathrm{s}})/(1-\nu_{\mathrm{s}})$, where ν_{s} denotes Possion's ratio of the solid matrix.

3.3. Consideration of ettringite formation at Scale II (cement-paste scale)

In addition to the prestress fields related to capillary depression and membrane forces outlined in the previous subsection, the crystallization pressure resulting from ettringite formation is taken into account (see Appendix A):

- During ettringite formation (see first stage of C_3A formation in Appendix A.2) new ettringite phases are introduced within the microstructure at the cement-paste scale [see Fig. 8(a)]. For the portion of ettringite forming within an infinitesimal time step $\mathrm{d}t$, the actual crystallization pressure is assigned, with $p = p_{C_6A\bar{S}_3H_{32}}([\mathrm{OH}^-](\xi))$ [see Eq. (9)]. The effect of changing deformation (shrinkage/expansion) on the prestress field is considered by adopting the pressure in previously formed ettringite domains, reading

$$p \to p - \langle A\rangle_{\mathrm{ettr}}\,\mathrm{d}(\operatorname{tr}\mathbf{E})k_{\mathrm{ettr}}. \tag{23}$$

In Eq. (23), $\langle A\rangle_{\mathrm{ettr}}$ denotes the volumetric average of the strain localization tensor in the ettringite phase embedded in the solid matrix [homogenized material of Scale Ib.2 (porous CSH)], with

$$\langle A\rangle_{\mathrm{ettr}} = \left[\left(1+S\frac{k_{\mathrm{ettr}}-k_{\mathrm{hom}}^{\mathrm{Ib.2}}}{k_{\mathrm{hom}}^{\mathrm{Ib.2}}}\right)\sum_r \frac{f_r}{1+S\frac{k_r-k_{\mathrm{hom}}^{\mathrm{Ib.2}}}{k_{\mathrm{hom}}^{\mathrm{Ib.2}}}}\right]^{-1}, \tag{24}$$

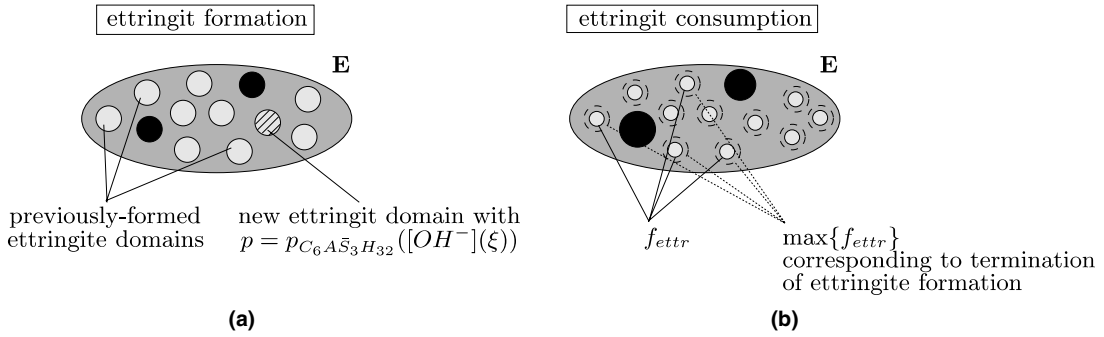

Fig. 8. Development of ettringite domains at Scale II in the course of C_3A hydration: (a) first stage and (b) second stage of C_3A hydration (f_{ettr} = volume fraction of ettringite).

where $r \in \{\text{ettr(ingite)}\ C_6A\bar{S}_3H_{32}, C\bar{S}H_2, C_4A\bar{S}H_{12}, C_3(A,F)H_6, CH,\ \text{anhydrous cement, porous CSH}\}$. In Eq. (24), S represents the Eshelby tensor $\mathbb{S}$, specialized for spherical inclusions embedded in the solid matrix giving $S = 1/3(1 + \nu_{\text{hom}}^{\text{Ib.2}})/(1 - \nu_{\text{hom}}^{\text{Ib.2}})$, where $\nu_{\text{hom}}^{\text{Ib.2}}$ denotes Poisson's ratio of the matrix [homogenized material of Scale Ib.2 (porous CSH)]. Finally, the homogenized prestress field due to crystallization pressure in consequence of ettringite formation is given by

$$\operatorname{tr}\boldsymbol{\Sigma}_{\text{ettr}} = -\langle A\rangle_{\text{ettr}} \int_0^{f_{\text{ettr}}} p\,\mathrm{d}f. \tag{25}$$

- For decreasing volume fraction of ettringite (see second stage of C_3A hydration in Appendix A.2) the homogenized stress tensor associated with the crystallization pressure is scaled by the ratio $f_{\text{ettr}}/\max\{f_{\text{ettr}}\}$, reading

$$\operatorname{tr}\boldsymbol{\Sigma}_{\text{ettr}} \to \frac{f_{\text{ettr}}}{\max\{f_{\text{ettr}}\}} \operatorname{tr}\boldsymbol{\Sigma}_{\text{ettr}}, \tag{26}$$

where $\max\{f_{\text{ettr}}\}$ represents the maximum volume fraction of ettringite attained at the end of the first stage of C_3A hydration (see Fig. 8).

3.4. Autogenous deformation at Scale II (cement-paste scale)

The differential change of the stress tensor[5] at a point $\mathbf{x}$ at the cement-paste scale results from changes of the strain tensor ($\mathrm{d}\boldsymbol{\varepsilon}$) and the prestress fields ($\mathrm{d}\boldsymbol{\sigma}_{\text{p}}$, $\mathrm{d}\boldsymbol{\sigma}_{\text{int}}$, and $\mathrm{d}\boldsymbol{\sigma}_{\text{ettr}}$), reading

$$\mathrm{d}\boldsymbol{\sigma}(\mathbf{x}) = \mathbb{c}(\mathbf{x}) : \mathrm{d}\boldsymbol{\varepsilon}(\mathbf{x}) + \mathrm{d}\boldsymbol{\sigma}_{\text{p}}(\mathbf{x}) + \mathrm{d}\boldsymbol{\sigma}_{\text{int}}(\mathbf{x}) + \mathrm{d}\boldsymbol{\sigma}_{\text{ettr}}(\mathbf{x}), \tag{27}$$

with $\mathbb{c}$ denoting the material tensor. Following *Levin's* theorem [47], the homogenized stress–strain relation takes the same form as Eq. (27), giving

$$\mathrm{d}\boldsymbol{\Sigma} = \mathbb{C}_{\text{hom}} : \mathrm{d}\mathbf{E} + \mathrm{d}\boldsymbol{\Sigma}_{\text{p}} + \mathrm{d}\boldsymbol{\Sigma}_{\text{int}} + \mathrm{d}\boldsymbol{\Sigma}_{\text{ettr}}, \tag{28}$$

where $\mathbb{C}_{\text{hom}}$ represents the homogenized material tensor at the cement-paste scale. Accounting for the stress-free boundary of the RVE in case of autogenous-shrinkage deformation only, giving $\mathrm{d}\boldsymbol{\Sigma} = \mathbf{0}$, the homogenized shrinkage strains at the cement-paste scale is finally obtained as

$$\mathrm{d}\mathbf{E} = -\mathbb{C}_{\text{hom}}^{-1} : \mathrm{d}\boldsymbol{\Sigma}_{\text{p}} + \mathrm{d}\boldsymbol{\Sigma}_{\text{int}} + \mathrm{d}\boldsymbol{\Sigma}_{\text{ettr}}, \tag{29}$$

or in volumetric form as

$$\mathrm{d}\epsilon = -\frac{1}{k_{\text{hom}}^{\text{II}}}\left(\mathrm{d}(\operatorname{tr}\boldsymbol{\Sigma}_{\text{p}}) + \mathrm{d}(\operatorname{tr}\boldsymbol{\Sigma}_{\text{int}}) + \mathrm{d}(\operatorname{tr}\boldsymbol{\Sigma}_{\text{ettr}})\right), \tag{30}$$

with $k_{\text{hom}}^{\text{II}}$ as the homogenized bulk modulus at Scale II. In contrast to $\operatorname{tr}\boldsymbol{\Sigma}_{\text{ettr}}$, which is available from Eqs. (25) and (26), $\operatorname{tr}\boldsymbol{\Sigma}_{\text{p}} + \operatorname{tr}\boldsymbol{\Sigma}_{\text{int}}$ appearing in Eq. (30) is obtained from the loading situation at Scale Ib.2 described in Subsection 3.2:

$$\operatorname{tr}\boldsymbol{\Sigma}_{\text{p}} + \operatorname{tr}\boldsymbol{\Sigma}_{\text{int}} = \langle A\rangle_{\text{m}} f_{\text{m}}(\operatorname{tr}\boldsymbol{\sigma}_{\text{p}} + \operatorname{tr}\boldsymbol{\sigma}_{\text{int}}), \tag{31}$$

where $\boldsymbol{\sigma}_{\text{p}}$ and $\boldsymbol{\sigma}_{\text{int}}$ are the homogenized prestress tensor and homogenized interface-stress tensors at Scale Ib.2 [see Eq. (20)]. In Eq. (31),

$$\langle A\rangle_{\text{m}} = \left[\sum_r \frac{f_r}{1 + S\frac{k_r - k_{\text{hom}}^{\text{Ib.2}}}{k_{\text{hom}}^{\text{Ib.2}}}}\right]^{-1}, \tag{32}$$

where $r \in \{\text{ettr(ingite)}\ C_6A\bar{S}_3H_{32}, C\bar{S}H_2, C_4A\bar{S}H_{12}, C_3(A,F)H_6, CH, \text{anhydrous cement, porous CSH}\}$.

[5] In order to account for the stress-free formation of hydrates [6], except for ettringite formation, an incremental stress–strain law is used.

3.5. Autogenous deformation at Scale III (mortar or concrete scale) according to [48]

The effective shrinkage deformation at Scale III due to the eigenstrain field in the matrix material "m" (cement paste, homogenized material of Scale II) is determined by the repeated use of *Hill's* lemma [48]. Hereby, the total strain field at a point $\mathbf{x}$ is divided into the elastic strain field $\boldsymbol{\varepsilon}^{\mathrm{el}}(\mathbf{x})$ and the eigenstrain field $\bar{\boldsymbol{\varepsilon}}(\mathbf{x})$:

$$\boldsymbol{\varepsilon}(\mathbf{x}) = \boldsymbol{\varepsilon}^{\mathrm{el}}(\mathbf{x}) + \bar{\boldsymbol{\varepsilon}}(\mathbf{x}). \tag{33}$$

The microscopic stress–strain law links $\boldsymbol{\varepsilon}^{\mathrm{el}}(\mathbf{x})$ to the stress field $\boldsymbol{\sigma}(\mathbf{x})$:

$$\boldsymbol{\sigma}(\mathbf{x}) = \mathbb{c}(\mathbf{x}) : \boldsymbol{\varepsilon}^{\mathrm{el}}(\mathbf{x}), \tag{34}$$

with $\mathbb{c}(\mathbf{x})$ denoting the material tensor. The elastic strain field is linked to the macroscopic or homogenized strain $\mathbf{E}$ via the strain localization tensor,

$$\boldsymbol{\varepsilon}^{\mathrm{el}}(\mathbf{x}) = \mathbb{A}(\mathbf{x}) : \mathbf{E}. \tag{35}$$

On the other hand, the macroscopic stress–strain law links the $\boldsymbol{\Sigma}$ and $\mathbf{E}$ via the homogenized material tensor $\mathbb{C}_{\mathrm{hom}}$

$$\boldsymbol{\Sigma} = \mathbb{C}_{\mathrm{hom}} : \mathbf{E}, \tag{36}$$

where $\boldsymbol{\Sigma} = \langle \boldsymbol{\sigma}(\mathbf{x}) \rangle$ and $\mathbf{E} = \langle \boldsymbol{\varepsilon}(\mathbf{x}) \rangle$. Inserting Eq. (35) into Eq. (34) and computing the volume average gives

$$\langle \boldsymbol{\sigma}(\mathbf{x}) \rangle = \boldsymbol{\Sigma} = \langle \mathbb{c}(\mathbf{x}) : \mathbb{A}(\mathbf{x}) : \mathbf{E} \rangle. \tag{37}$$

Inserting Eq. (36) into Eq. (37) and applying *Hill's* lemma [Eq. (12)] two times gives

$$\mathbb{C}_{\mathrm{hom}} : \mathbf{E} = \langle \mathbb{c}(\mathbf{x}) : \mathbb{A}(\mathbf{x}) \rangle : \mathbf{E} = \langle \mathbb{c}(\mathbf{x}) : \mathbb{A}(\mathbf{x}) \rangle : \langle \boldsymbol{\varepsilon}(\mathbf{x}) \rangle = \langle \mathbb{c}(\mathbf{x}) : \mathbb{A}(\mathbf{x}) : \boldsymbol{\varepsilon}(\mathbf{x}) \rangle. \tag{38}$$

Inserting Eq. (33) into Eq. (38) gives

$$\mathbb{C}_{\mathrm{hom}} : \mathbf{E} = \langle \mathbb{c}(\mathbf{x}) : \mathbb{A}(\mathbf{x}) : \boldsymbol{\varepsilon}^{\mathrm{el}}(\mathbf{x}) \rangle + \langle \mathbb{c}(\mathbf{x}) : \mathbb{A}(\mathbf{x}) : \bar{\boldsymbol{\varepsilon}}(\mathbf{x}) \rangle. \tag{39}$$

Accounting for the symmetry of $\mathbb{c}(\mathbf{x})$ and $\mathbb{A}(\mathbf{x})$, with $c_{ijkl} = c_{klij}$ and $A_{ijkl} = A_{klij}$, the first term on the right-hand side of Eq. (39) becomes after applying *Hill's* lemma a third time

$$\langle \mathbb{A}(\mathbf{x}) : \mathbb{c}(\mathbf{x}) : \boldsymbol{\varepsilon}^{\mathrm{el}}(\mathbf{x}) \rangle = \langle \mathbb{A}(\mathbf{x}) : \boldsymbol{\sigma}(\mathbf{x}) \rangle = \langle \mathbb{A}(\mathbf{x}) \rangle : \langle \boldsymbol{\sigma}(\mathbf{x}) \rangle = \mathbb{I} : \boldsymbol{\Sigma}. \tag{40}$$

Accounting for stress the free boundary in Eq. (40), $\boldsymbol{\Sigma} = \mathbf{0}$, Eq. (39) can be written as

$$\mathbb{C}_{\mathrm{hom}} : \mathbf{E} = \langle \mathbb{A}(\mathbf{x}) : \mathbb{c}(\mathbf{x}) : \bar{\boldsymbol{\varepsilon}}(\mathbf{x}) \rangle. \tag{41}$$

Finally, specializing Eq. (41) for eigenstrains $\mathrm{d}\bar{\boldsymbol{\varepsilon}}_{\mathrm{m}}$ in the matrix material, with $\mathrm{d}\bar{\boldsymbol{\varepsilon}}_{\mathrm{m}} = \mathrm{d}\mathbf{E}^{\mathrm{II}}$ as determined in Subsection 3.5 [Eq. (29)], gives access to the homogenized shrinkage strains as

$$\mathrm{d}\mathbf{E} = \mathbb{C}_{\mathrm{hom}}^{-1} : \langle \mathbb{A} \rangle_{\mathrm{m}} : \mathbb{c}_{\mathrm{m}} : \mathrm{d}\mathbf{E}^{\mathrm{II}}, \tag{42}$$

where the subindex "m" refers to the matrix material [homogenized material at Scale II (cement paste)]. In volumetric form, Eq. (42) becomes

$$\mathrm{d}\epsilon^{s} = f_{\mathrm{m}} \frac{k_{\mathrm{hom}}^{\mathrm{II}}}{k_{\mathrm{hom}}^{\mathrm{III}}} \langle A \rangle_{\mathrm{m}} \, \mathrm{d}(\mathrm{tr}\mathbf{E}^{\mathrm{II}}), \tag{43}$$

with $k_{\mathrm{hom}}^{\mathrm{II}}$ and $k_{\mathrm{hom}}^{\mathrm{III}}$ as the homogenized bulk moduli at Scale II (cement-paste scale) and Scale III (mortar or concrete scale), respectively, and

$$\langle A \rangle_{\mathrm{m}} = \left[\sum_{r} \frac{f_r}{1 + S \frac{k_r - k_{\mathrm{hom}}^{\mathrm{II}}}{k_{\mathrm{hom}}^{\mathrm{II}}}} \right]^{-1}, \tag{44}$$

where $r \in \{\mathrm{aggregate}, \mathrm{cement\ paste}\}$.

4. Model validation: autogenous-shrinkage experiments

For the validation of the multiscale model for autogenous deformations of cement-based materials outlined in the previous section, a uniaxial test setup was employed [24]. Hereby the autogenous deformation is measured in the direction of a flexible corrugated plastic mould, which holds the cement paste and is placed in the measuring frame (see Fig. 9). The deformation is monitored by a displacement gauge located at one end of the mould. The chosen experimental setup permits commencement of the measurement shortly after casting, giving access to the time of setting, i.e., the percolation threshold.

4.1. Materials

In the experimental program, OPCs characterized by different *Blaine* (grinding) finenesses Ø were considered. The mineralogy of the cement-clinker—gypsum compound is given in Table 2. The Bogue calculation [42] gives access to the mass fraction m_x of each clinker phase and gypsum, see Table 3. The grain-size distributions, including the medium radius of the clinker grains R, the cumulative pore-size distributions obtained from MIP, and calorimetry results of the considered OPCs are given in Fig. 10.

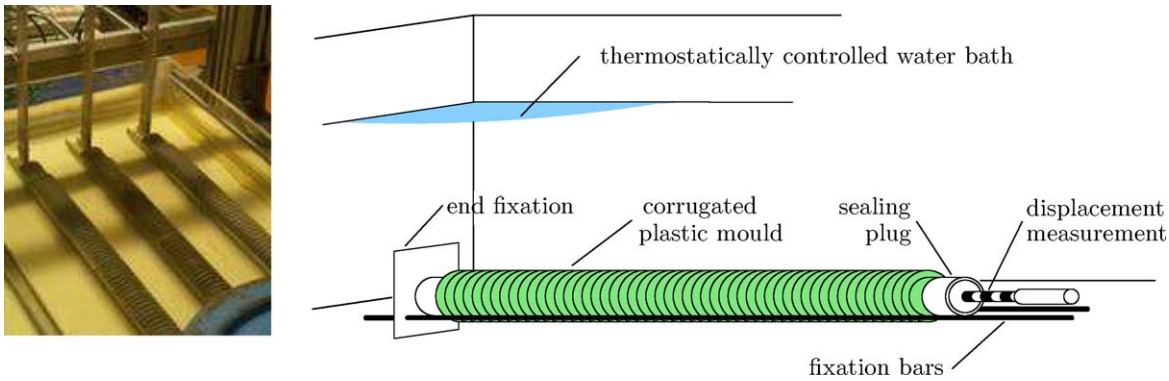

Fig. 9. Experimental setup for uniaxial measurements of autogenous deformation.

Table 2
Mineralogy of cement-clinker—gypsum compound considered in the experiment program

Component	Mass-%
OPC clinker	
SiO_2	20.27
Al_2O_3	4.48
Fe_2O_3	2.19
CaO	61.37
MgO	1.46
SO_3	0.90
Na_2O_3	0.25
K_2O	0.76
TiO_2	0.22
P_2O_5	0.27
Cr_2O_3	0.01
MnO	0.05
Ignition loss	0.37
Sulfate provider	
$CaSO_4 \cdot 2H_2O$	4.93
$CaSO_4 \cdot 1/2H_2O$	2.47

Table 3
Mass fractions of clinker phases

Component	m_x [mass-%]
C_3S	62.51
C_2S	10.97
C_3A	8.17
C_4AF	6.66
Gypsum + halfhydrate	7.40
Others	4.29

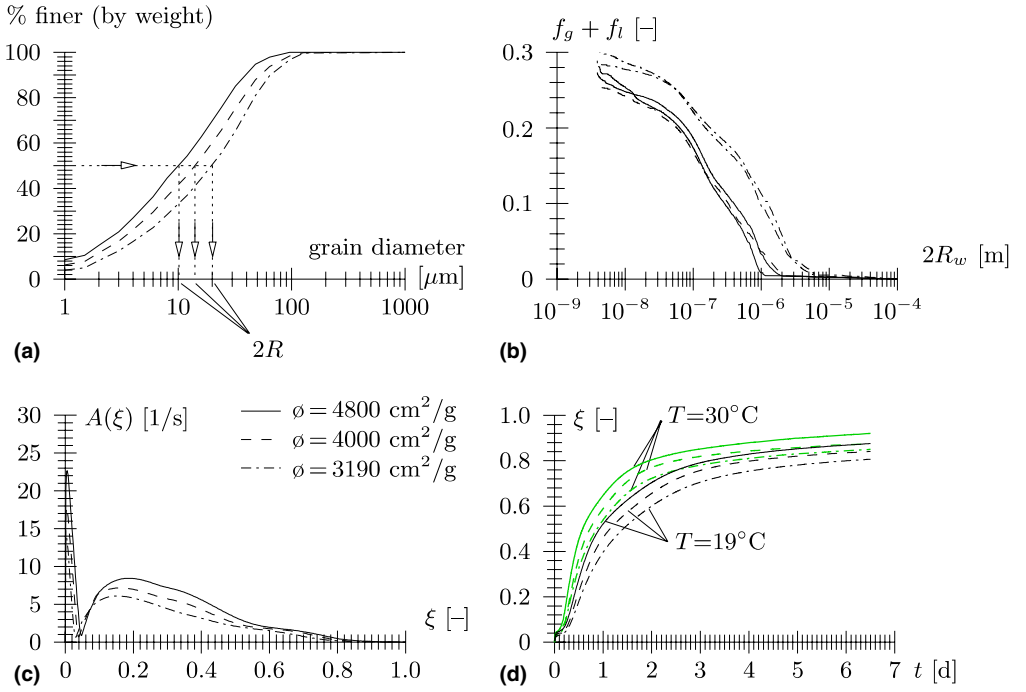

Fig. 10. Characterization of OPCs considered in experimental program: (a) grain-size distributions (Ø = Blaine fineness, R = medium radius of clinker grains), (b) cumulative pore-size distributions obtained by MIP, testing cement paste with $w/c = 0.42$ and age = 28 days, (c) chemical affinity $A(\xi)$ obtained from differential-calorimetry results, and (d) evolution of overall degree of hydration ξ for isothermal conditions using $A(\xi)$ depicted in (c).

4.2. Presentation of results

The uniaxial test equipment used for the experiment study provides the length change of the specimens as a function of time. In order to relate this length change to the hydration extent, the chemical affinity was determined experimentally from the obtained calorimetric-test results (see Fig. 10(c)). Based on the heat release monitored during the differential-calorimetry test, $Q(t)$, the evolution of the hydration extent is computed from specializing the thermal problem to isothermal conditions (the isothermal test temperature in the calorimeter was 30 °C) as

$$-L_\xi \dot{\xi}(t) = -\dot{Q}(t) \quad \Rightarrow \quad \xi(t) = \frac{Q(t)}{L_\xi}, \tag{45}$$

where L_ξ [J] denotes the heat of hydration of the cement considered in the test sample. Inserting $\dot{\xi} = \dot{Q}/L_\xi$ from Eq. (45) into a suitable *macroscopic* evolution law for the hydration kinetics [44], the evolution of the the chemical affinity A [1/s] related to the overall hydration extent is obtained as

$$\dot{\xi}(t) = A(t)\exp\left[-\frac{E_a}{\mathscr{R}T}\right] \quad \Rightarrow \quad A(t) = \frac{\dot{Q}(t)}{L_\xi \exp[-E_a/(\mathscr{R}T)]} \ [1/s], \tag{46}$$

where E_a, $\mathscr{R}$, and T denote the apparent activation energy of the employed cement, the universal gas constant, and the absolute temperature, respectively. Combination of $\xi(t)$ and $A(t)$ as computed from Eqs. (45) and (46) gives access to the chemical-affinity function $A(\xi)$ which, in turn, when applied to the isothermal conditions of the autogenous-shrinkage experiment ($T = 19\ °C = \text{constant}$), gives access to the evolution of the hydration extent within the specimens of the autogenous-shrinkage experiments [see Fig. 10(d)].

Figs. 11–13 show the shrinkage deformation as a function of time and as a function of the hydration extent ξ. The circles in Figs. 11(a), 12(a), and 13(a) mark the time instant t_0 corresponding to the percolation of the solid phase (percolation threshold), also referred to as setting time. For $t < t_0$, the cement paste can shrink freely and, hence, the *Le Chatelier* contraction is converted directly into a macroscopically observable shrinkage strain. In Figs. 11(a), 12(a), and 13(a), $t = 0$ refers to the time instant of water addition. Moreover, ε^s was shifted such that $\varepsilon^s(t = t_0) = 0$. From the obtained experimental results, the following conclusions can be drawn:

- All specimens show a clear expansion period right after setting, which is attributed to the crystallization pressure of ettringite.
- Once ettringite formation is terminated (end of second stage in C_3A hydration), shrinkage is governed by capillary depression in the pore liquid.
- The smaller the w/c-ratio, the earlier shrinkage is initiated. This is explained by the lower liquid saturation in specimens with small w/c-ratios.

Figs. 11(b), 12(b), and 13(b) show a comparison between the evolution of $\varepsilon^s(\xi)$ obtained from the experimental study and $\varepsilon^s(\xi) = \epsilon^s(\xi)/3$ predicted by the multiscale model (Sections 2 and 3, Appendix A). As regards

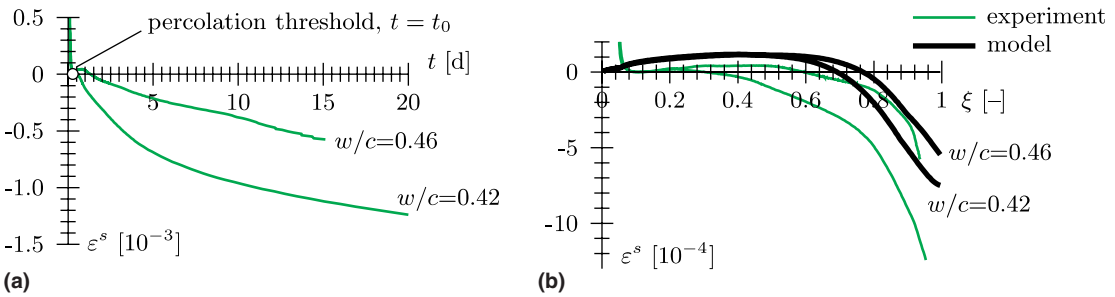

Fig. 11. Shrinkage experiments for OPC paste ($\phi = 4800\ cm^2/g$): history of shrinkage strain ε^s as a function of (a) time and (b) the hydration extent.

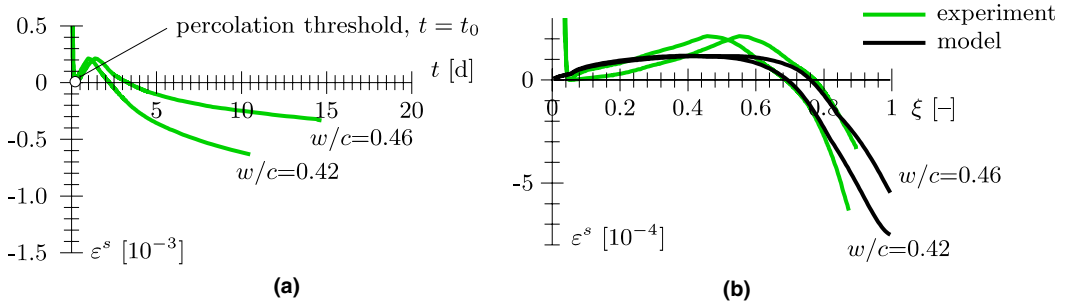

Fig. 12. Shrinkage experiments for OPC paste ($\phi = 4000\ cm^2/g$): history of shrinkage strain ε^s as a function of (a) time and (b) the hydration extent.

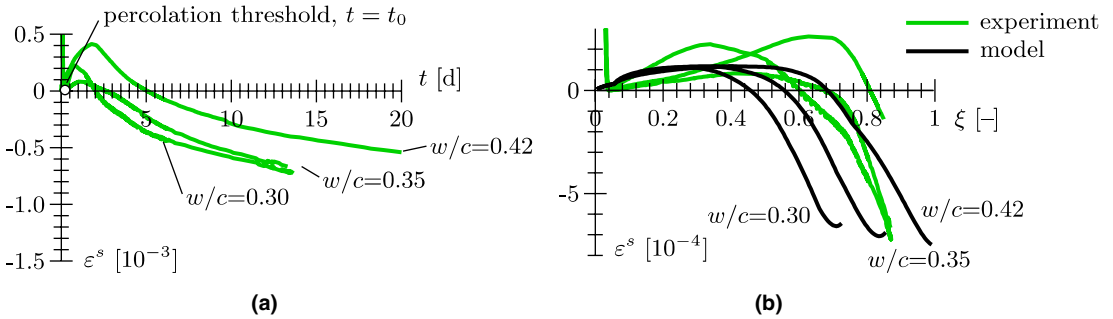

Fig. 13. Shrinkage experiments for OPC paste ($\phi = 3190\ \mathrm{cm^2/g}$): history of shrinkage strain ε^s as a function of (a) time and (b) the hydration extent.

the model prediction, homogenization of elastic properties (bulk moduli k_r and shear moduli μ_r) was performed using the intrinsic elastic properties of the cement clinker and hydrate phases given in [7]. For upscaling of the autogenous-shrinkage deformation, the small time scale for short-term creep of CSH at Scale Ib.1, when compared to the time scale of the hydration process, is taken into account by using the stiffness representing both the elastic and the viscous material response,

$$E = \frac{9k\left(\frac{1}{\mu_0} + \frac{1}{\mu_v}\right)^{-1}}{3k + \left(\frac{1}{\mu_0} + \frac{1}{\mu_v}\right)^{-1}}. \tag{47}$$

In Eq. (47) $k = 13.9$ GPa and $\mu_0 = 8.8$ GPa are the elastic parameters and $\mu_v \approx 1/3\mu_0$ refers to the stiffness of a Kelvin-Voigt element used to describe deviatoric creep.

5. Application: hybrid analysis of shotcrete tunnel linings

The presented multiscale model is employed in the context of hybrid analyses of shotcrete tunnel linings [29]. In the present application, one measurement cross-section (MCS) of the Lainzer tunnel near Vienna, which is part of the high-capacity railway from Vienna to Salzburg, is investigated (MCS at km 8.340 of track 9). The geometric dimensions of the standard cross-section of the Lainzer tunnel are given in Fig. 14. The necessary input parameters for the multiscale model and the hydration kinetic model (Appendix A) are

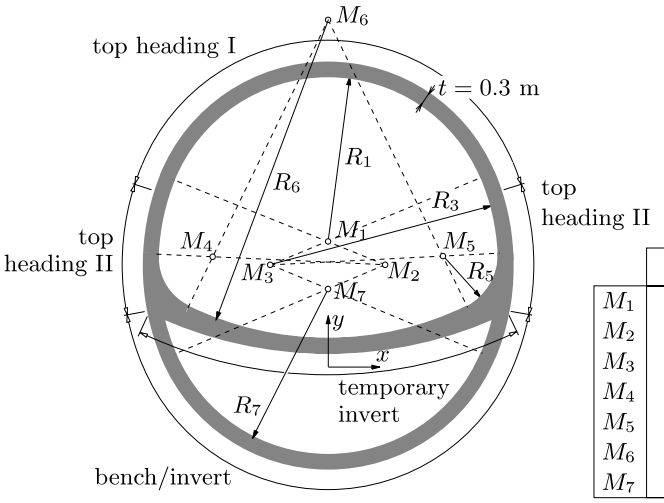

R_1	4.74
R_2	6.39
R_3	6.39
R_4	1.50
R_5	1.50
R_6	8.50
R_7	4.44

	x [m]	y [m]
M_1	0	3.40
M_2	1.52	2.77
M_3	-1.52	2.77
M_4	-3.06	3.00
M_5	3.06	3.00
M_6	0	9.30
M_7	0	2.14

Fig. 14. Lainzer tunnel: cross-section.

summarized in Table 4, giving access to the intrinsic material functions for Young's modulus $E(\xi)$, Poisson's ratio $\nu(\xi)$, and autogenous-shrinkage strain $\varepsilon^s(\xi)$ (see Fig. 15). The intrinsic material functions for strength growth and creep, on the other hand, are obtained from macroscopic experiments, see [29].

Fig. 16 shows the construction history for track 9 of the Lainzer tunnel. The reference time $t = 0$ is defined as the time instant at the beginning of construction at the considered MCS, i.e., the excavation of the top heading I, which took place on January 23, 2001. 370 hours after the erection of top heading I, the excavation was interrupted for almost 69 days.

5.1. Thermochemical analysis

The hydration kinetic model outlined in Appendix A is used to determine to the history of the hydration extents $\xi_x(t,r)$ and the temperature $T(t,r)$ in the lining, where r represents the radial coordinate. Hereby, the

Table 4
Input parameters for multiscale model for the shotcrete employed at the Lainzer tunnel

Scale II (cement-paste scale)	
Water/cement-ratio	0.48
Blaine fineness of cement	4895 cm^2/g
Average initial radius of clinker grains	5 μm
Mass fractions of clinker phases in cement	
C_3S	48.7%
C_2S	22.8%
C_3A	11.4%
C_4AF	9.4%
$C\bar{S}H_2$	7.7%
Scale III (shotcrete scale)	
Volume fraction of aggregate	70%
Young's modulus aggregate	50 GPa
Poisson's ratio aggregate	0.3

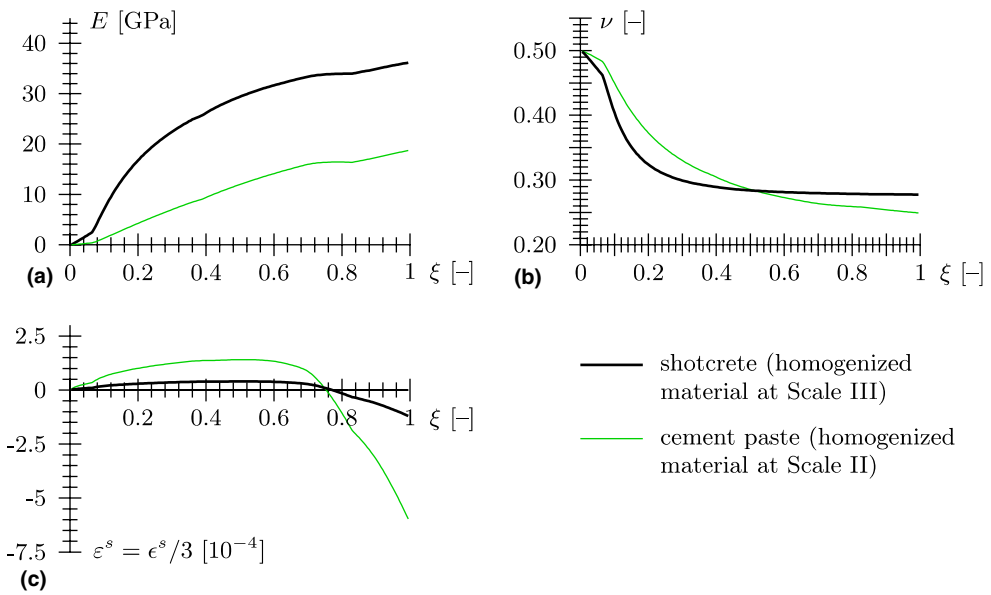

Fig. 15. Intrinsic material function employed in hybrid analysis: (a) Young's modulus, (b) Poisson's ratio, and (c) autogenous-shrinkage strains.

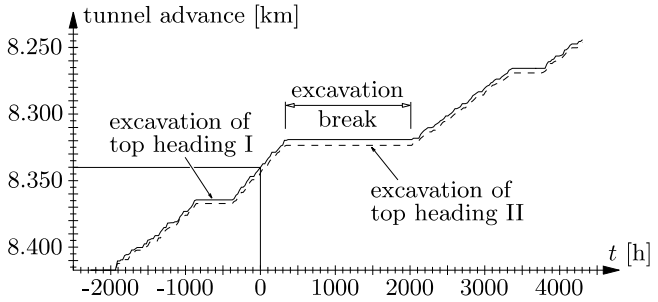

Fig. 16. Lainzer tunnel: construction history of "Bierhäuselberg" tunnel containing track 9.

different chemical reactions and their heat release are considered in the field equation of the thermal problem, reading

$$\rho c\dot{T} - \sum_x l_{\xi x}\dot{\xi}_x = -\mathrm{div}\,\mathbf{q}, \tag{48}$$

where (ρc) [kJ/(K m^3)] denotes the volume heat capacity, and $l_{\xi x}$ [kJ/m^3] represents the heat release of the xth hydration reaction, $\mathbf{q}$ [kJ/(m^2 h)] is the heat flow vector. It is related to the temperature via Fourier's law of heat conduction:

$$\mathbf{q} = -k\,\mathrm{grad}\,T, \tag{49}$$

where k [kJ/(m h)] denotes the thermal conductivity. At the inner surface of the lining, a radiation-type boundary condition is considered, with

$$\mathbf{q}\cdot\mathbf{n} = \alpha(T - T^{\infty}). \tag{50}$$

The employed material parameters used in the thermochemical analysis are summarized in Table 5. The output of the thermochemical analysis, i.e., the fields $\xi(t,r)$ and $T(t,r)$, serve as input for the mechanical analysis of the considered MCS. The evolution of the temperature obtained at the centre of the shotcrete lining shows a steep increase up to 65 °C within the first 12 h, which agrees well with the temperature measurements performed at the construction site [see Fig. 17(b)]. Thereafter, the temperature approaches the stationary situation, which is reached within the first week after application of the lining. In contrast to previous presentations of results obtained from thermochemical analyses of shotcrete linings [38,28], the w/c-ratio, which enters the hydration model (see Appendix A), affects the temperature increase in the lining. The higher the w/c-ratio, the more water is available for the hydration process, reflected by an increased hydration rate [7] resulting in a higher temperature rise in the lining.

5.2. Mechanical analysis

The temperature field and the fields of the reaction extents serve as input for the subsequent mechanical analysis. Hereby, the strain within each point of the lining is accessible via interpolation of displacement histories available at the so-called measurement points. This strain field together with the actual temperature and

Table 5
Material parameters and initial temperatures used in the thermochemical analysis

	Shotcrete	Soil
Density ρ [kg/m^3]	2400	1450
Heat capacity c [kJ/(kg K)]	0.88	0.88
Thermal conductivity k [kJ/(m h K)]	3.6	4.6
Radiation coefficient α [kJ/(m^2 h K)]	40	–
Initial temperature T_0 [°C]	16	10
Temperature in tunnel opening T^{∞} [°C]	18	–

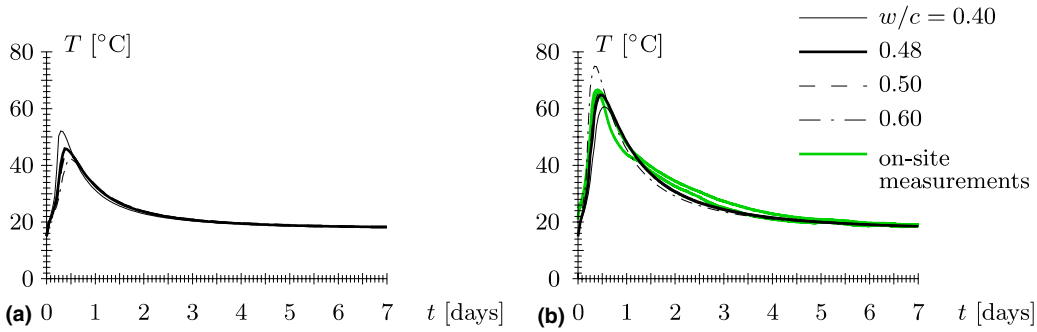

Fig. 17. Temperature history at (a) the inner surface and (b) the centre of the lining.

reaction extents are considered in a multi-surface chemoplasticity model, accounting for aging elasticity, autogenous-shrinkage deformations, strength growth, microcracking, and creep (for details, see [27,29]). For the interpretation of the numerical results obtained from the hybrid analysis of the considered measurement cross-section, the level of loading $\mathscr{L}$ is introduced. It amounts to 0% for the unloaded structure and to 100% when the stresses reach the (actual) compressive strength. For the underlying Drucker–Prager criterion, the level of loading at a point in the shotcrete lining is determined from

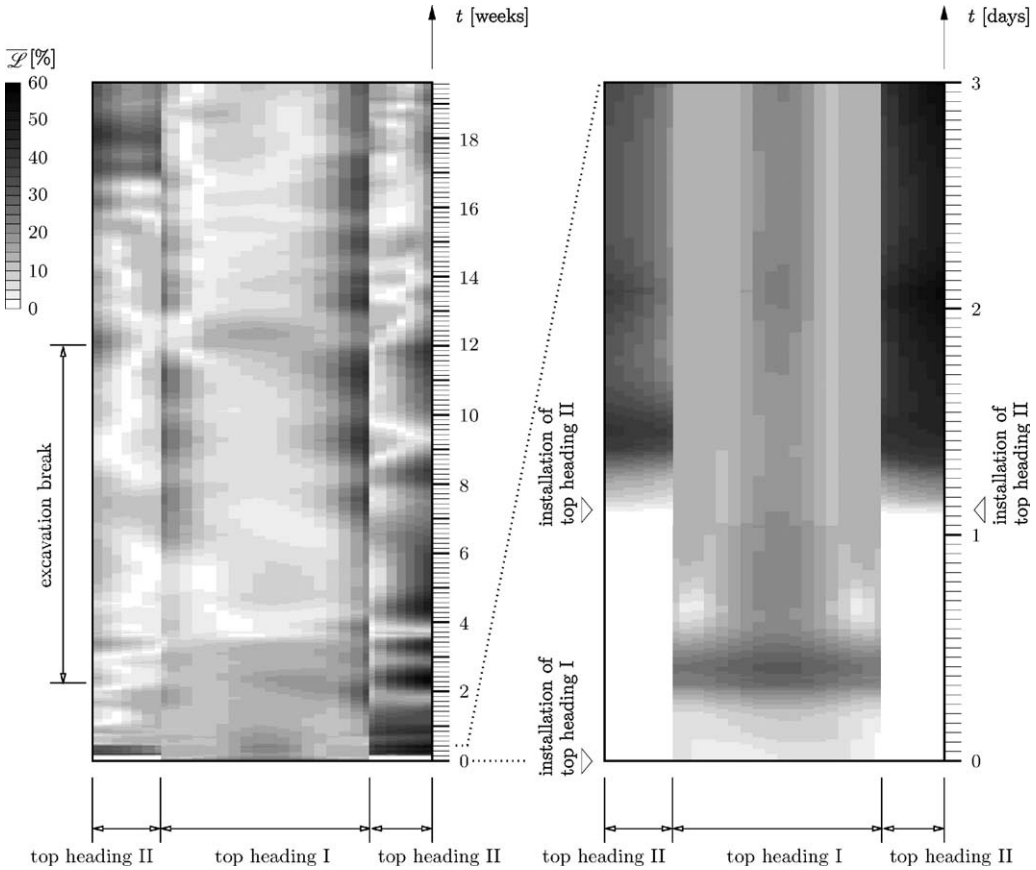

Fig. 18. History of distribution of $\overline{\mathscr{L}}$ in shotcrete lining at considered MCS (top view): for a time span of (a) 4.5 month and (b) 3 days after application ($t = 0$ refers to the time instant of installation of top heading I).

$$\mathscr{L} = \frac{\sqrt{J_2(\sigma_\varphi, \sigma_z)} + \alpha I_1(\sigma_\varphi, \sigma_z)}{f_c(\xi)/\beta}, \tag{51}$$

where σ_φ and σ_z are the stress component in the circumferential and longitudinal direction of the tunnel. In Eq. (51), $I_1(J_2)$ represents the first (second) invariant of the stress tensor (deviator). α and β are constant parameters (see [29]).

For illustration purposes, the level of loading is averaged over the shell thickness, with $\overline{\mathscr{L}} = \int_h \mathscr{L}\,\mathrm{d}r$. Fig. 18 shows the evolution of $\overline{\mathscr{L}}$ over the first 4.5 months. The increase of the level of loading within the first 12 h [see Fig. 18(b)] is caused by thermal dilation associated with the temperature rise in the course of the hydration process. This is observed for all newly installed parts of the lining, i.e., top heading I and the top heading II on both the left and the right side. Cooling of the lining and creep deformations lead to a decrease of the level of loading after the first 12 h. Based on the measurements, and also reflected by the distribution of the level of loading, the MCS started to move towards the right bench, leading to a continuous, high loading of the right part of the lining. In fact, the surface settlements associated with this movement were the reason to stop the tunnel advance 370 h after installation of the considered cross-section. During this construction break, the footings of the existing top heading II were improved by installing micropiles of 80 mm diameter. Because of this, continuation of tunnel excavation after the construction break resulted only in slight increases of the measured displacement.

However, the hydration process, which continued during the construction break, increased the stiffness of the lining. Thus, the rather small displacement change after continuation of the excavation process resulted in an increase of the level of loading, as observed in the top heading I [see Fig. 18(a)].

6. Conclusions and outlook on future work

In this paper, a multiscale micromechanics model for the prediction of autogenous-shrinkage deformations of cement-based materials is presented. It combines continuum micromechanics with advanced cement hydration models. Moreover, it enables a sound incorporations of the finer-scale origin of autogenous deformations, i.e., capillary depression and ettringite formation pressure. The developed multiscale model was assessed by means of shrinkage experiments at the so-called cement-paste scale and applied within a macroscopic (structural) analysis of a shotcrete tunnel lining. The advantages of incorporating finer-scale information in structural analysis, as motivated by this paper, is twofold:

- The macroscopic material properties can be related to intrinsic properties of the constituents, i.e., properties which do not change from one cement-based material to the other, and to the mixture characteristics (w/c-ratio, aggregate volume fraction). Accordingly, the mixture characteristics of the shotcrete used at the investigated tunnel site directly entered the hybrid analysis scheme.
- Having established a link between mixture characteristics and cement chemistry, on the one hand, and the macroscopic performance of cement-based materials, on the other hand, performance-based optimization of cement-based materials becomes possible (e.g., optimization of shotcrete as regards the level of loading during tunnel advances).

Even though the attained multiscale model was capable of reproducing experimental results and providing necessary information for macroscopic analyses, further model improvements as regards cement hydration and the description of the mechanical behavior are topic of ongoing research:

- In order to improve the employed kinetic law and, thus, the prediction of the volume fraction of ettringite, calorimetric studies focusing on the hydration C_3A in the presence of gypsum are currently performed.
- In this paper, the creep deformations in consequence of eigenstresses (capillary depression and crystallization pressure) was taken into account by an increased compliance during homogenization of the creep-active phases. For the description of the creep deformations resulting from macrostress application (external loading), on the other hand, a macroscopic formulation was employed. Ongoing work focuses

on the extension of the presented multiscale framework to creep. For this purpose, the CSH-creep compliance is currently deduced from indentation experiments. Upscaling of this finer-scale creep behavior will provide access to the macroscopic creep compliance.

Acknowledgements

The authors are indebted to E. Schön and R. Friedle (LAFARGE Centre Technique Europe Central GmbH, Mannersdorf, Austria) for providing the cements employed in the experiments reported in Section 4, R.A. Cook and K.C. Hover for communication of data of MIP experiments [13], and F.-J. Ulm (Massachusetts Institute of Technology, Cambridge, MA, USA) for valuable comments on multiscale modeling. Financial support by the Austrian Science Fund (FWF) via project P15912-N07 is gratefully acknowledged.

Appendix A. Hydration model

For determination of the volume fractions of the phases of early-age cement paste, the following set of stoichiometric reactions are employed for the four main clinker phases of Portland cement, i.e., tricalcium silicate (C_3S), dicalcium silicate (C_2S), tricalcium aluminate (C_3A) and tetracalcium aluminate ferrite (C_4AF) [43]:

$$C_3S + 5.3H \rightarrow 0.5C_{3.4}S_2H_8 + 1.3CH \tag{52}$$

$$C_2S + 4.3H \rightarrow 0.5C_{3.4}S_2H_8 + 0.3CH \tag{53}$$

$$C_4AF + 2CH + 10H \rightarrow 2C_3(A,F)H_6 \tag{54}$$

$$C_3A + 3C\bar{S}H_2 + 26H \rightarrow C_6A\bar{S}_3H_{32} \tag{55}$$

$$C_3A + 0.5C_6A\bar{S}_3H_{32} + 2H \rightarrow 1.5C_4A\bar{S}H_{12} \tag{56}$$

$$C_3A + CH + 12H \rightarrow C_4AH_{13} \tag{57}$$

Eqs. (55)–(57) describe the formation of calcium aluminate hydrates from C_3A in the presence of gypsum, which is added to prevent rapid setting of C_3A. Initially, C_3A reacts with gypsum to form ettringite [Eq. (55)]. After all gypsum is consumed, C_3A reacts with the previously formed ettringite to form monosulfoaluminates [Eq. (56)]. Following depletion of the ettringite supply, C_3A reacts with portlandite CH (one of the products of C_3S and C_2S hydration). The hydration extent is described by the degree of hydration of the clinker phases, ξ_{C_3S}, ξ_{C_2S}, ξ_{C_3A}, and ξ_{C_4AF}. The evolution of $\xi_x (x \in C_3S, C_2S, C_4AF)$ is controlled by induction, nucleation, and growth until $\xi_x = \bar{\xi}_x$, and diffusion limited kinetics thereafter [7]. The aforementioned three stages of C_3A hydration are diffusion limited [40].

For the description of the hydration kinetics of C_3S, C_2S, and C_4AF, kinetic laws given in [7], including the Avrami law for nucleation and growth kinetics, and the Fuji and Kondo model [18] for diffusion limited kinetics, are employed. Whereas the first and the third stage of C_3A hydration are characterized by a thickening barrier layer (ettringite and C_4AH_{13}, respectively, around the anhydrous C_3A grain) and, hence, by a decreasing reaction rate, the second is dominated by a thinning barrier layer (ettringite) with an increasing reaction rate.

Based on the stoichiometric reactions given in Eqs. (52)–(57), and the molar masses $\mathscr{M}$, and densities ρ of the different phases given in [43] (see Table 6), the volume fractions of the different phases can be determined as a function of the hydration degree ξ_x and the mass fractions of the clinker phases m_x. This is shown exemplarily for the volume fraction of $C_{3.4}S_2H_8$ appearing in Eqs. (52) and (53):

$$f_{C_{3.4}S_2H_8}(t) = \left[\xi_{C_3S}(t)\frac{m_{C_3S}}{\mathscr{M}_{C_3S}}\frac{0.5\mathscr{M}_{C_{3.4}S_2H_8}}{\rho_{C_{3.4}S_2H_8}} + \xi_{C_2S}(t)\frac{m_{C_2S}}{\mathscr{M}_{C_2S}}\frac{0.5\mathscr{M}_{C_{3.4}S_2H_8}}{\rho_{C_{3.4}S_2H_8}}\right]\bar{\rho} \tag{58}$$

with $\bar{\rho} = \sum_x \frac{\rho_x}{m_x} + \frac{\rho_H}{w/c}\sum_x \frac{1}{m_x}$.

Table 6
Molar masses $\mathscr{M}$ and densities ρ of the different phases given in cement paste (taken from [43])

		Density ρ [kg/m^3]	Molar mass $\mathscr{M}$ [kg/mol]
Tricalcium silicate	C_3S	3150	0.228
Dicalcium silicate	C_2S	3280	0.172
Tricalcium aluminate	C_3A	3030	0.270
Tetracalcium aluminate ferrite	C_4AF	3730	0.486
Water	H	998	0.018
Gypsum	$C\bar{S}H_2$	2320	0.172
Calcium hydroxide	CH	2240	0.074
Hydrogarnet	$C_3(A,F)H_6$	2670	0.407
Trisulfate ettringite	$C_6A\bar{S}_3H_{32}$	1750	1.255
Monosulfate	$C_4A\bar{S}H_{12}$	1990	0.623
Calcium aluminate hydrate	C_4AH_{13}	2050	0.560
Calcium silicate hydrate	$C_{3.4}S_2H_8$	1990	0.454

A.1. Hydration kinetics of C_3S, C_2S, and C_4AF according to [7]

In this subsection, the kinetic laws used in [7] are shortly summarized. The evolution equation for the degree of hydration reads

$$\frac{\mathrm{d}\xi_x}{\mathrm{d}t} = \frac{1}{\tau_x(T,\phi)}\widetilde{A}(\xi_x), \tag{59}$$

where $\widetilde{A}$ [–] is the normalized chemical affinity, τ_x [h] denotes the characteristic time of the the chemical reaction, which depends on temperature T and Blaine fineness ϕ. According to [7], three stages of the hydration process can be distinguished:

1. Dissolution of clinker ($t < t_{x0}$ and $\xi < \xi_{x0}$): modeled with a constant reaction rate, i.e., $\widetilde{A} = 1$ and

$$\tau_x(T,\phi) = \frac{t_{x0}}{\xi_{x0}}\frac{\phi_0}{\phi}\exp\left[\frac{E_{ax}}{\mathscr{R}}\left(\frac{1}{T}-\frac{1}{T_0}\right)\right], \tag{60}$$

   with $T_0 = 293$ K and $\phi_0 = 3602$ cm^2/g. For isothermal conditions, i.e., $T = \text{const}$, ξ_x can be written as

$$\xi_x = \xi_{x0}\frac{t}{t_{x0}}\frac{\phi}{\phi_0}\exp\left[-\frac{E_{ax}}{\mathscr{R}}\left(\frac{1}{T}-\frac{1}{T_0}\right)\right]. \tag{61}$$

2. Nucleation and growth kinetics ($\xi_{x0} < \xi_x < \bar{\xi}_x$ and $t_{x0} < t < \bar{t}_x$): for this period the Avrami model is employed, reading

$$-\ln[1-(\xi_x-\xi_{x0})] = \left\{k\frac{\phi}{\phi_0}\exp\left[-\frac{E_{ax}}{\mathscr{R}}\left(\frac{1}{T}-\frac{1}{T_0}\right)\right](t-t_{x0})\right\}^{\kappa}, \tag{62}$$

   where k is the rate constant, and

$$\widetilde{A} = \frac{1-(\xi_x-\xi_{x0})}{\{-\ln[1-(\xi_x-\xi_{x0})]\}^{\frac{1}{\kappa}-1}}, \quad \tau_x(T,\phi) = \frac{1}{\kappa k}\frac{\phi_0}{\phi}\exp\left[\frac{E_{ax}}{\mathscr{R}}\left(\frac{1}{T}-\frac{1}{T_0}\right)\right]. \tag{63}$$

   For isothermal conditions, i.e., $T = \text{const}$, ξ_x can be written as

$$\xi_x = \xi_{x0} + 1 - \exp\left\{-\left[k\frac{\phi}{\phi_0}\exp\left[-\frac{E_{ax}}{\mathscr{R}}\left(\frac{1}{T}-\frac{1}{T_0}\right)\right](t-t_{x0})\right]^{\kappa}\right\}. \tag{64}$$

3. Diffusion limited kinetics ($\xi_x > \bar{\xi}_x$ and $t > \bar{t}_x$): the rate-controlling mechanism is the diffusion of dissolved ions, through a thickening layer of hydration products, to the anhydrous clinker grain. [18] state the following relation for ξ_x:

$$(1-\xi_x)^{1/3} = -\frac{(2D)^{1/2}}{R}(t-\bar{t}_x)^{1/2} + (1-\bar{\xi}_x)^{1/3}, \tag{65}$$

where D is the diffusion coefficient, R is the average initial radius of the cement-clinker grain. From Eq. (65) follows:

$$\widetilde{A} = \frac{(1-\xi_x)^{2/3}}{(1-\bar{\xi}_x)^{1/3} - (1-\xi_x)^{1/3}} \quad \text{and} \quad \tau_x(T,\phi) = \frac{R^2}{3D}\frac{\phi_0}{\phi}\exp\left[\frac{E_{ax}}{\mathscr{R}}\left(\frac{1}{T}-\frac{1}{T_0}\right)\right]. \tag{66}$$

For isothermal conditions, i.e., $T = \text{const}$, ξ_x can be written as

$$\xi_x = 1 - \left[-\frac{(2D)^{1/2}(t-\bar{t}_x)^{1/2}}{R\left\{\exp\left[\frac{E_{ax}}{\mathscr{R}}\left(\frac{1}{T}-\frac{1}{T_0}\right)\right]\right\}^{1/2}(\phi_0/\phi)^{1/2}} + (1-\bar{\xi}_x)^{1/3}\right]^3. \tag{67}$$

A.2. Hydration kinetics of C_3A

According to [40] the hydration of C_3A in the presence of gypsum can be separated into three stages which are all diffusion controlled:

1. In the first stage, C_3A reacts with gypsum to form ettringite [Eq. (55)] around the C_3A grains. The diffusion of sulfate ions through the thickening ettringite barrier layer towards the anhydrous C_3A grain is the rate-controlling mechanism.
2. After all gypsum is consumed, the second stage, characterized by the dissolution of the formed ettringite layer and C_3A species and the subsequent formation of monosulfoaluminates [Eq. (56)]. The rate of reaction increases since ions diffuse through a thinning ettringite barrier layer. Following depletion of the ettringite supply, the anhydrous C_3A particle is again exposed.
3. Finally, in the third stage, C_3A reacts with portlandite CH (a crystalline product of C_3S and C_2S hydration) to form calcium aluminate hydrates [Eq. (57)]. Once again, the thickening barrier layer of the latter renders the third stage of C_3A hydration to be diffusion limited.

The hydration kinetics of the three stages of C_3A hydration may be derived from isothermal calorimetry (see, e.g., [8]) or X-ray diffraction and differential thermal analysis (DTA) (see, e.g., [35]). In [8], the duration of ettringite formation [first stage, see Eq. (55)] for an equimolar C_3A–$C\bar{S}H_2$, mixture is given as 7 and 8 days, depending if hydration is taking place in water or saturated CH solution, respectively (isothermal temperature of 25 °C, Blaine fineness 3300 cm^2/g), while the second stage, i.e., ettringite conversion to monosulfate once the gypsum is consumed, lasted for additional two days. In [35], on the other hand, the duration of ettringite formation reaction for an equimolar mixture was given by 3 and 12 h, for the hydration taking place in suspension (water) and paste (water, $w/c = 0.5$), respectively.

In lack of a suitable evolution law, constant reaction rates were assumed for Eqs. (55)–(57).

A.3. Overall degree of hydration ξ

ξ is obtained from the values of ξ_x determined from the kinetic laws outlined in Appendices A.1 and A.2 as

$$\xi = \frac{\sum_x m_x \xi_x}{\sum_x m_x}, \tag{68}$$

where $x \in \{C_3S, C_2S, C_3A, C_4AF, C\bar{S}H_2\}$ and m_x are the mass fractions of the four clinker phases and gypsum. $\xi_{C\bar{S}H_2}$ is linearly coupled to ξ_{C_3A} [see Eq. (55)].

References

[1] Acker P. Micromechanical analysis of creep and shrinkage mechanisms. In: Ulm F-J, Bažant ZP, Wittmann FH, editors. Concreep 6: proceedings of the 6th international conference on creep, shrinkage & durability mechanics of concrete and other quasi-brittle materials. Amsterdam, Cambridge, USA: Elsevier Science Ltd.; 2001. p. 15–25.

[2] Acker P, Ulm F-J. Creep and shrinkage of concrete: physical origins and practical measurements. Nucl Engng Des 2001;203:148–58.

[3] Aldrian W. Beitrag zum Materialverhalten von früh belastetem Spritzbeton [Contribution to the material behavior of early loaded shotcrete. PhD thesis, University of Leoben, Leoben, Austria, 1991 [in German].

[4] Aydan O, Sezaki M, Kawamoto T. Mechanical and numerical modelling of shotcrete. In: Pande GN, Pietruszcak S, editors. Numerical methods in geomechanics. Rotterdam, The Netherlands: Balkema; 1992. p. 757–64.

[5] Baroghel-Bouny V, Mainguy M, Lassabatere T, Coussy O. Characterization and identification of equilibrium and transfer moisture properties for ordinary and high-performance cementitious materials. Cement Concrete Res 1999;29:1225–38.

[6] Bažant ZP. Thermodynamics of solidifying or melting viscoelastic material. J Engng Mech Div (ASCE) 1979;105(6):933–52.

[7] Bernard O, Ulm F-J, Lemarchand E. A multiscale micromechanics-hydration model for the early-age elastic properties of cement-based materials. Cem Concr Res 2003;33:1293–309.

[8] Brown PW. Kinetics of tricalcium aluminate and tetracalcium aluminoferrite hydration in the presence of calcium sulfate. J Am Ceram Soc 1993;76(12):2971–6.

[9] Bye GC. Portland cement. 2nd ed. London: Thomas Telford Publishing; 1999.

[10] Chateau X, Dormieux L. Homogenization of a non-saturated porous medium: Hill's lemma and applications. C.R. Acad Sci II 1995; 320:627–34 [in French with abridged english version].

[11] Chateau X, Dormieux L. Micromechanics of saturated and unsaturated porous media. Int J Numer Anal Methods Geomech 2002;26: 831–44.

[12] Cohen MD. Theories of expansion in sulfoaluminate-type expansive cements: schools of thought. Cem Concr Res 1983;13:809–18.

[13] Cook RA, Hover KC. Mercury porosimetry of hardened cement paste. Cem Concr Res 1999;29:943–93.

[14] de Borst R, van den Boogaard AH. Finite-element modelling of deformation and cracking in early-age concrete. J Engng Mech (ASCE) 1995;120(12):2519–34.

[15] Diamond S. Review mercury porosimetry: an inappropriate method for the measurement of pore size distributions in cement-based materials. Cem Concr Res 2000;30:1517–25.

[16] Diamond S, Leeman ME. Pore size distribution in hardened cement paste by SEM image analysis. In: Diamond S, Mindess S, Glasser FP, Roberts LR, Skalny JP, Wakely LD, editors. Microstructure of cement-based systems/bonding and interfaces in cementitious materials, vol. 370. Pittsburgh: Materials Research Society; 1995. p. 217–26.

[17] Eijk RJ, Brouwers HJH. Prediction of hydroxyl concentrations in cement pore water using a numerical hydration model. Cem Concr Res 2000;30:1801–6.

[18] Fuji K, Kondo W. Kinetics of the hydration of tricalcium silicate. J Am Ceram Soc 1974;57:492–502.

[19] Gaydos J, Boruvka L, Rotenberg Y, Chen P, Neumann AW. Applied surface thermodynamics. New York: Dekker; 1996.

[20] Hershey AV. The elasticity of an isotropic aggregate of anisotropic cubic crystals. J Appl Mech (ASME) 1954;21:236–40.

[21] Hofstetter G, Mang HA. Computational mechanics of reinforced and prestressed concrete structures. Braunschweig, Wiesbaden: Vieweg; 1995.

[22] Hua C, Acker P, Ehrlacher A. Analyses and models of the autogenous shrinkage of hardening cement paste I. Modelling at macroscopic scale. Cem Concr Res 1995;25:1457–68.

[23] Jehng J-Y, Sprague DT, Halperin WP. Pore structure of hydrating cement paste by magnetic resonance relaxation analysis and freezing. Magn Reson Imaging 1996;14:785–91.

[24] Jensen OM, Freiesleben Hansen P. A dilatometer for measuring autogenous deformation in hardening Portland cement paste. Mater Struct 1995;28(181):69–76.

[26] Kroener E. Berechnung der elastischen Konstanten des Vielkristalls aus den Konstanten des Einkristalls [Computation of the elastic constants of a polycrystal based on the constants of the single crystal]. Zeitschrift für Physik 1958;151:504–18 [in German].

[27] Lackner R, Hellmich Ch, Mang HA. Constitutive modeling of cementitious materials in the framework of chemoplasticity. Int J Numer Methods Engng 2002;53(10):2357–88.

[28] Lackner R, Mang HA. Modeling of early-age fracture of shotcrete: application to tunneling. In: Karihaloo BL, editor. Proceedings of the IUTAM symposium on analytical and computational fracture mechanics of non-homogeneous materials. Dordrecht, Cardiff, Wales: Kluwer Academic Publishers; 2002. p. 197–210.

[29] Lackner R, Mang HA. Cracking in shotcrete tunnel shells. Engng Fract Mech 2003;70:1047–68.

[30] Larbi JA, Fraay LA, Bijen JM. The chemistry of the pore fluid of silica fume blended cement systems. Cem Concr Res 1990;20: 506–16.

[31] Mang HA, Lackner R, Meschke G, Mosler J. Computational modeling of concrete structures. In: Karihaloo BL, Ritchie RO, Milne I, de Borst R, Mang HA, editors. Comprehensive structural integrity. Numerical and computational methods, vol. 3. Oxford: Elsevier Science; 2003. p. 541–606.

[32] Meschke G. Consideration of aging of shotcrete in the context of a 3D viscoplastic material model. Int J Numer Methods Engng 1996;39:3123–43.

[33] Milia F, Fardis M, Papavassiliou G, Leventis A. NMR in porous materials. Magn Reson Imaging 1998;16:677–8.

[34] Mori T, Tanaka K. Average stress in matrix and average elastic energy of materials with misfitting inclusions. Acta Metall 1973;21: 571–4.

[35] Mosalamy FH, Shater MA. Hydration mechanism of tricalcium aluminate with gypsum at 1:1 mole ratio at low water/solid ratio and in suspension. Thermochim Acta 1984;74:113–21.
[36] Nemat-Nasser S, Hori M. Micromechanics: overall properties of heterogeneous materials, vol. 37. Amsterdam: North-Holland; 1993.
[37] Niu Y-Z, Tu C-L, Liang R-Y, Zhang S-W. Modelling of thermomechanical damage of early-age concrete. J Engng Mech (ASCE) 1995;121(4):717–26.
[38] Pichler Ch, Lackner R, Spira Y, Mang HA. Thermochemomechanical assessment of ground improvement by jet grouting in tunneling. J Engng Mech (ASCE) 2003;129(8):951–62.
[39] Ping X, Beaudoin JJ. Mechanism of sulphate expansion II: validation of thermodynamic theory. Cem Concr Res 1992;22:845–54.
[40] Pommersheim J, Chang J. Kinetics of hydration of tricalcium aluminate in the presence of gypsum. Cem Concr Res 1988;18:911–22.
[41] Schubert P. Beitrag zum rheologischen Verhalten von Spritzbeton [Contribution to the rheological behavior of shotcrete]. Felsbau, 6, 1988.
[42] Taylor HFW. Cement chemistry. 2nd ed. London: Thomas Telford Publishing; 1997.
[43] Tennis PD, Jennings M. A model for two types of calcium silicate hydrate in the microstructure of portland cement pastes. Cem Concr Res 2000;30:855–63.
[44] Ulm F-J, Coussy O. Modeling of thermochemomechanical couplings of concrete at early ages. J Engng Mech (ASCE) 1995;121(7): 785–94.
[45] Ulm F-J, Coussy O. Strength growth as chemo-plastic hardening in early age concrete. J Engng Mech (ASCE) 1996;122(12):1123–32.
[46] Van den Bogert PAJ, de Borst R, Nauta P. Simulation of the mechanical behaviour of young concrete. In: IABSE, editor, Computational Mechanics of Concrete Structures, vol. 54, ETH-Zürich, 1987. IABSE Colloquium Delft 1987, p. 339–47.
[47] Zaoui A. Structural morphology and constitutive behaviour of microheterogenous materials. In: Suquet P, editor. Continuum micromechanics. Vienna: Springer; 1997.
[48] Zaoui A. Continuum micromechanics: survey. J Engng Mech (ASCE) 2002;128:808–16.